Spatial-temporal Power Management of 5G Base Station Microgrids with Dynamic Backup Energy Storage

Yingqi Zhu, *Student Member, IEEE*, Kang Li, *Senior Member, IEEE*, and Li Zhang, *Senior Member, IEEE*

***Abstract*—As fifth-generation (5G) networks expand and communication traffic surges, optimizing base station microgrids (BSMGs) to improve renewable energy utilization and reduce operational costs has become essential for meeting global decarbonization targets. To address the challenges posed by renewable generation variability in power management, three techniques are employed to evaluate five different Copula functions for modeling and analyzing the dependence structure between random variables, independent of their marginal distributions. These techniques are the grey relational analysis (GRA) optimized by the triangular fuzzy analytic hierarchy process (TF-AHP), criteria importance analysis based on inter-criteria correlations (CRITIC), and the entropy weight method (EWM). Subsequently, a spatiotemporal energy management model is developed to reduce base station (BS) power consumption while accounting for communication constraints related to bandwidth, transmission rate, and quality of service (QoS). Dynamic backup energy storage capacity for BSs is then incorporated into zonal scheduling to manage regional traffic fluctuations. The proposed approach is validated on the IEEE 33-node test system, and simulation results confirm that it significantly lowers BS power consumption, achieving up to 5.18% in energy savings and up to a 63.6% reduction in required backup power capacity, thereby significantly enhancing the overall energy efficiency and flexibility of BSMGs.**

***Index Terms*—Base station microgrids, renewable generation, energy management, backup energy storage.**

I. INTRODUCTION

THE surge in mobile data traffic driven by the rise of the Internet of Things (IoT) has accelerated the adoption of the fifth generation (5G) communication networks [1]-[3]. The number of 5G base stations (BSs) in 2024 is roughly six times the figure recorded in 2020, reflecting a rapid growth trend. By 2024, the number of 5G BSs worldwide surpassed 6 million, serving over 2 billion users and achieving a 25% penetration rate [4], [5]. BSs are the primary contributors to energy consumption in cellular wireless networks, accounting for approximately 70% of the total network energy usage [6], [7]. There is increasing interest in creating base station microgrids (BSMGs) by outfitting BSs with local renewable generators and energy storage (ES) to lower carbon footprints and improve energy efficiency [8]-[11]. Existing 5G BS energy management systems (EMSs) remain suboptimal, resulting in inefficiencies and underutilized backup storage. Moreover, as the secure and reliable operation of BSs is highly dependent on the distribution grid, power outages or local faults can lead to severe service degradation and even large-scale communication interruptions. Recent major power grid failures worldwide show that inadequate backup energy directly threatens radio access network (RAN) availability and service continuity. For example in April 2025, the unprecedented power blackout in Iberian Peninsula triggered concurrent mobile network failures across multiple regions, confirming that existing backup power systems at RAN sites were insufficient to maintain availability during a prolonged, large-scale power disruption. These events provide documented evidences that inadequate backup energy provisioning directly threatens RAN availability and service continuity. Therefore, improving the resilience of BS power supply through coordinated use of distributed renewable generation and backup ES is crucial for stable 5G network operation.

5G BSs require greater bandwidth and massive antenna arrays, increasing the network's power demand to nearly two to three times that of 4G systems [12]-[14]. Optimal operation of the 5G networks relies heavily on analyzing the dynamic spatiotemporal distribution of communication loads and implementing energy-saving techniques while ensuring service quality. The rapid growth of BS deployment has intensified both the spatial and temporal variability of communication loads, making energy-efficient and resilient operation increasingly challenging. To cope with the fluctuating renewable generation and dynamic user demands, next-generation BSs are being integrated with renewable energy sources (RESs) such as wind and photovoltaic (PV) power, together with local base station energy storage (BSES) units. This configuration forms a BSMG that can locally balance supply and demand, improve energy utilization, and enhance power-supply reliability during distribution network failures. However, current BSES units are often designed as passive emergency backups, leading to underutilization and low economic return during normal grid operation. Major grid failures, however, present a pivotal opportunity to integrate these systems into active energy management. This shift would enhance service resilience while unlocking the latent value of idle backup capacity.

To address these challenges, this paper proposes a

The authors are with the School of Electronic and Electrical Engineering, University of Leeds, LS2 9JT Leeds, U.K. (e-mail: elyzhu@leeds.ac.uk, k.li1@leeds.ac.uk, l.x.zhang@leeds.ac.uk).

Copyright (c) 2026 IEEE. Personal use of this material is permitted. However, permission to use this material for any other purposes must be obtained from the IEEE by sending a request to pubs-permissions@ieee.org.

comprehensive optimization framework for 5G BSMGs that integrates renewable uncertainty modeling, user–BS association, BSES capacity evaluation, and partitioned scheduling. A Copula-driven probabilistic approach is first employed to characterize the correlated stochastic nature of wind and solar power outputs. By generating a probability-weighted set of renewable generation scenarios, this method effectively captures underlying uncertainties, and these scenarios are subsequently fed into the microgrid scheduling model to enable probabilistic assessment of scheduling decisions across the scenario set. Next, a user–BS association strategy is optimized by jointly considering spatial distribution, temporal variation, and communication constraints to minimize overall BS power consumption. Using the IEEE 33-bus system for validation, node vulnerability and BSES backup capacity are quantitatively evaluated from topological, electrical, and statistical perspectives. Finally, a partitioned scheduling method that distinguishes between work and residential areas is proposed to reduce operational costs while maximizing renewable energy utilization. The proposed framework effectively enhances both the energy efficiency and power-supply resilience of 5G BSMGs.

The major contributions of this paper are summarized as follows:

1) A Copula-based stochastic scenario generation approach is proposed to model the uncertainty of wind and PV outputs. Five Copula functions are evaluated using an improved grey relational analysis (GRA) method to identify the most suitable one, ensuring that realistic and representative input data are selected for BSMG scheduling optimization.
2) A user–BS association optimization framework is established by considering spatial, temporal, and communication constraints. This method minimizes the total BS power consumption by dynamically balancing user distribution across BSs.
3) The BSES backup capacity configuration is optimized based on topology, electrical parameters, and statistical indicators using the IEEE 33-bus system as a case study. The results show that reducing BS power demand effectively decreases required backup capacity while enhancing system dispatchability and grid interaction potential.
4) A partitioned scheduling strategy is proposed to minimize the BSMG operating costs while maximizing the renewable energy utilization. By separately optimizing work and residential regions, the approach significantly improves RES utilization and reduces operational costs compared with traditional mixed scheduling methods.

The remainder of the paper is organized as follows. Section II reviews the related work. In Section III, the problem formulation is given. The multi-objective scheduling model is proposed in Section IV. In Section V, the case study and simulation results are presented and analyzed. Finally, Section VI concludes the paper.

II. RELATED WORKS

Recent studies have concentrated on enhancing the energy efficiency of communication BSs through the implementation of dynamic sleep modes, refined power control algorithms, and optimal user association strategies. Israr et al. [15] proposed a resource-on-demand approach for small cell BSs, integrating advanced sleep modes with energy cooperation to optimize energy saving of 5G infrastructure. To optimize energy utilization in 5G BSs, a novel distributed PV DC microgrid structure is proposed together with an energy management strategy using the curve fitting–perturb and observe–incremental conductance (CF-P\&O-INC) maximum power point tracking (MPPT) algorithm, considering both the energy and information flows [16]. Fayad and Cinkler [17] addressed the joint user and power allocation problem in 5G millimeter-wave networks, formulating it as an integer linear programming model and developing a genetic algorithm (GA)–based heuristic approach to reduce BS power consumption while maintaining user Quality of Service (QoS). Their results demonstrated significant improvements in energy efficiency and the number of switched-off BSs compared with benchmark methods. While these studies have successfully demonstrated the potential to lower energy consumption across various traffic conditions and maintain the stable operation of BSMGs, little has been done to consider both the service quality and user experience, in particular, the role of backup ES in the BS energy supply system.

In addition to the communication-side optimization, the literature has increasingly focused on the coordinated scheduling of ES in 5G BSMGs [18], [19]. Efficient utilization and intelligent dispatch of ES are essential for enhancing energy efficiency, maintaining microgrid stability, and supporting renewable energy integration [20]-[22]. However, backup ES units at BSs often remain underutilized for long periods, leading to significant resource idleness. To address this issue, Dai et al. [23] proposed a distributed collaborative optimization framework that considers both communication load migration and dynamic ES operation to exploit the flexibility of 5G BSs. Peng et al. [24] developed a coordinated day-ahead scheduling framework that integrates 5G BS load migration, storage utilization, and electrical vehicle (EV) charging management, demonstrating effective reduction in network energy consumption and enhanced supply reliability. Zhang et al. [25] developed a bi-level joint optimization model to minimize capacity planning and operational costs of shared energy storage (SES) systems in large-scale BS networks. Moreover, some studies have explored integrating distributed BSES resources into auxiliary power markets for frequency regulation and peak-shaving services, demonstrating their economic potential for network operators. However, most existing works still treat BSES operation and communication management as separate problems. A comprehensive framework that jointly optimizes backup capacity, load conditions, and energy usage is still missing, which motivates the proposal of an integrated BSMG scheduling model in this study.

In addition to energy efficiency and storage scheduling, network resilience has emerged as a key research area in communication systems. Prior studies as summarized in [26] largely address service continuity via backup power, renewable integration, and energy-aware management during

power disruptions. For example, Cabrera-Tobar et al. [27] examine ES regulation strategies for 5G BSs with explicit reliability considerations, and Wu et al. [28] evaluate 5G network resilience through Petri-net models and resilient scheduling mechanisms. Nevertheless, resilience remains under-explored in the context of BSMG operational scheduling under renewable generation uncertainty and dynamic user behavior, leaving a gap in understanding how stochastic energy availability affects 5G BSMG operational robustness and reliability.

Despite significant progresses have been made in improving the energy efficiency and flexibility of 5G BS operations, several research gaps remain. First, most existing studies address communication-side optimization and energy management separately, overlooking the coupling between user association, renewable integration, and storage utilization in BSMGs. Second, while distributed ES and RES have been incorporated into BS networks, their backup and dispatchable capabilities are often underutilized, limiting their potential contribution to power supply resilience under distribution grid failures. Furthermore, network resilience has received limited attention at the operational level and is seldom incorporated into coordinated scheduling and energy management frameworks for BSMGs. Third, few studies have explored comprehensive scheduling frameworks that jointly consider spatial load characteristics, renewable generation variability, and the dynamic interaction between work and residential areas. Finally, the probabilistic nature of renewable energy is often oversimplified, leading to unrealistic or less robust scheduling results. Table I compares existing studies in terms of their methods, main focuses, key contributions, and limitations.

TABLE I
COMPARISON OF EXISTING STUDIES

Paper	Method	Main focus	Contribution	Limitation
[15]	Resource-on-demand sleep-mode control	5G small-cell energy saving	Renewable sharing with advanced BS sleep modes	Fixed BS clusters with no BSES backup evaluation
[16]	CF-P&O-INC MPPT and energy management	PV-based 5G BS DC microgrid	Improves PV tracking and DC-bus stability	Local PV control without BSMG-level scheduling
[17]	Integer linear programming and GA	5G millimeter-wave user and power allocation	Jointly optimizes user allocation, power, and BS on/off states	Communication-side saving only without energy-side scheduling
[18]	Stochastic energy model and traffic offloading	Renewable-powered 5G HetNet	Integrates renewable supply, traffic offloading, and sleep modes	Energy buffering only without dynamic BSES backup scheduling
[19]	HOMER-based techno-economic optimization	Hybrid energy systems for base transceiver stations (BTS) sites	Optimizes PV, wind, diesel, and battery sizing across climates	Long-term site planning without operational BSES dispatch
[20]	Dispatchable-capacity evaluation with cone programming	BS backup batteries for voltage regulation	Uses time-varying backup capacity to improve voltage profiles	Grid voltage control only without BSMG operation
[21]	State-space aggregation with model predictive control	BS backup storage for frequency support	Coordinates BS sleep control and battery operation	Treats BSs as grid-response resources rather than BSMG units
[22]	Dispatch-boundary estimation with rule-based control	BS backup batteries for frequency regulation	Estimates spare battery capacity while keeping backup reliability	Frequency-support focus without microgrid energy scheduling
[23]	Distributed collaborative optimization	Distribution network and 5G BS coordination	Combines load migration and dynamic backup ES to reduce cost	No renewable uncertainty modeling or partitioned BSMG scheduling
[24]	Day-ahead cone programming with task migration	Distribution-network scheduling with 5G BSs and EVs	Coordinates task migration and EV charging to lower cost and losses	EV-focused flexibility without BSES backup assessment
[25]	Bi-level planning with decomposition	SES for PV-integrated 5G BSs	Lowers BS costs through storage leasing	Does not assess backup capability of individual BS batteries
[26]	Literature review	Telecom energy resilience	Reviews backup power, renewables, microgrids, and energy management	Review-level summary without BSMG scheduling model
[27]	Time-of-use battery dispatch	5G BS battery reliability	Uses reserve capacity to dispatch idle batteries and reduce cost	Price-arbitrage focus without BSMG-level coordination
[28]	Petri-net resilience evaluation	5G network resilience under attacks	Compares scheduling strategies to reduce traffic loss	Cyber-resilience focus without energy-backup modeling

III. PROBLEM FORMULATION

Table II summarizes the principal mathematical notations employed in the proposed modeling framework. For the sake of readability, the table includes only the key variables, auxiliary symbols are defined in context alongside their respective equations.

A. Flowchart of the Proposed Methodology

To clearly illustrate the logical framework of the proposed study, the overall workflow is presented in Fig. 1. The process starts by generating representative wind and PV output scenarios. The optimal Copula is then selected using an improved GRA procedure that integrates one subjective and two objective weighting schemes. Next, a user–BS association mechanism is optimized to reduce BS power consumption under spatiotemporal and communication constraints. Then the backup and dispatchable capacities of BSES are evaluated considering load levels and node vulnerability of the distribution network. Finally, a multi-objective scheduling model is formulated to minimize the operating cost while maximizing renewable-energy utilization.

TABLE II
DEFINITION OF NOTATION

Notation	Definition
i, j, k, t	Indices of BSs, users, nodes, and periods
n, N	Number of samples, indicators, users, or nodes
X_i, x	Observed wind/PV sample and generation value
$F(x_i), f(x_i)$	Marginal distribution and density functions
$C(\cdot), c(\cdot)$	Copula connection function and density function
θ	Copula parameter vector
τ, ρ, d^2	Kendall correlation, Spearman correlation, and squared Euclidean distance

$\log\delta(\theta, u, v)$	Copula log-likelihood value
D_0	Grey relational score
$S_{i,t}$	Working status of BS i
$Z_{i,j,t}$	BS-user connection variable
$P_{i,t}^{SG}$	Total power consumption of BS i
L_j, $L_{i,t}$, $L_{\max}$	User demand, BS load, and maximum BS load
B, $B_{i,t}$, $B_{\max}$	User bandwidth demand, allocated bandwidth, and maximum bandwidth
$P_{i,t}^{tr}$, $P_{\max}^{tr}$	BS transmission power and maximum value
$g_{i,j}$, $d_{i,j}$	Channel gain and BS-user distance
N_0	Channel white noise
$X_i^{backup}(t)$, T_i^{backup}	Required BSES capacity and backup time
V_k, d_k, T_0	Node vulnerability, load level, and minimum backup time
$M_D(k)$, $C_C(k)$, $M_B(k)$	Degree, closeness, and betweenness centrality
H	Initial network efficiency
$G(k)$	Modified Gini coefficient
$P_{t,ch}$, $P_{t,dis}$	BSES charging and discharging power
$S_{t,ch}$, $S_{t,dis}$	BSES charging and discharging states
$E_s(t)$	BSES energy capacity
η	BSES charging and discharging efficiency
P_t^{grid} , $P_{pv}(t)$, $P_{pw}(t)$	Grid exchange, PV, and wind power
$P_{load}(t)$	Load demand
π_t	Time-of-use electricity price
$\lambda_{grid}^{'}$, $\lambda_{ES}^{'}$, $\lambda_{net}^{'}$	Grid cost, BSES cost, and total BSMG cost
λ	Renewable energy utilization rate
ω_1, ω_2	Weights of cost and renewable utilization

B. Generation of Representative Wind and PV Power Output Scenarios

The variability of RES poses significant challenges for power system scheduling. Modelling the wind and PV output fluctuations requires the generation of representative scenarios to reflect their uncertainties accurately. These scenarios are essential for effective microgrid scheduling, as they help simulate realistic operating conditions under uncertainties. Although scheduling is typically performed over a 24-hour period, the results can vary greatly depending on the selected day. Choosing representative days is crucial because they ensure that the generated scenarios capture typical RES output patterns, improving the reliability and generalizability of scheduling decisions. However, limited research has addressed the issue of selecting suitable representative days for the scheduling.

Copula functions are powerful tools for modeling the dependencies among random variables, making them particularly effective for generating representative scenarios that capture the joint variability of wind power and PV preserving key statistical characteristics, thereby enabling more efficient scheduling decisions [29]. Ju et al. [30] applied Copula functions to model wind–PV correlations for risk-based analysis, but did not compare different Copula types or incorporate scenario generation into scheduling.

Using kernel density estimation, the contribution of a sample to the estimated probability density function value $\hat{f}(x)$ is determined by calculating the distance between each observed sample X and the target generation value x. Let $X_1, X_2, \cdots, X_n$ be independent and identically distributed samples representing the observed hourly wind or PV generation data. The variable x corresponds to a possible generation level within the same hour for which the probability density function $\hat{f}(x)$ is to be estimated.

$$\hat{f}(x) = \frac{1}{nh}\sum_{i=1}^{n} K\left(\frac{x - X_i}{h}\right) \tag{1}$$

$$F(x_1, x_2, \cdots, x_n) = C(F(x_1), F(x_2), \cdots, F(x_n)) \tag{2}$$

$$f(x_1, x_2, \cdots, x_n) = c(f(x_1), f(x_2), \cdots, f(x_n)) \cdot \prod_{n=1}^{N} f_n(x_n) \tag{3}$$

where K is the kernel function, h is the window width, n is the number of variables, $F(x_i)(i = 1, 2, \cdots, n)$ is the marginal distribution function, $f(x_i)(i = 1, 2, \cdots, n)$ is the marginal density function, $F(x_1, x_2, \cdots, x_n)$ is the joint distribution function of n variables, $f(x_1, x_2, \cdots, x_n)$ is the joint probability density function of n variables, $C(\cdot)$ is the Copula connection function, and $c(\cdot)$ is the Copula density function.

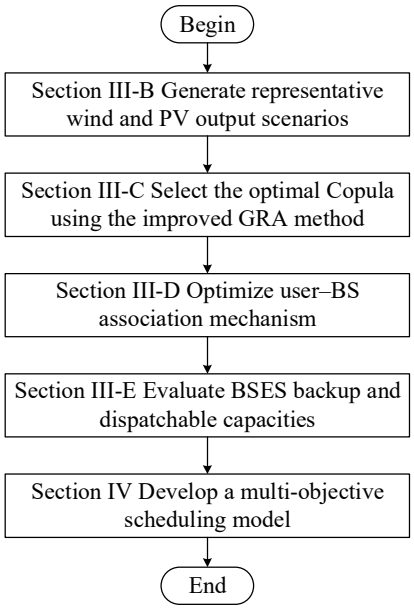


Fig. 1. Flowchart of the proposed methodology.

To capture the diurnal periodicity of renewable generation, the above estimation is performed separately for each hour of the day. For hours with negligible PV output (typically nighttime), PV is treated as zero deterministically, and only wind power is modeled. This ensures that the hourly probability distribution reflects both the stochastic nature and temporal variation of renewable generation.

Copulas fall into two families: Archimedean and Elliptic. Archimedean Copulas include Gumbel, Clayton, and Frank, while Elliptic Copulas mainly include Gaussian and t-Copula [31], [32]. Evaluating goodness of fit and related metrics is essential to select the optimal function.

To evaluate the fitting performance and dependency characteristics of different Copula functions, six statistical indicators are employed as shown in Eqs. (4)–(12). Akaike Information Criterion (AIC) compares Copula models by balancing goodness of fit with model complexity, while the Bayesian Information Criterion (BIC) emphasizes penalizing

complexity, particularly with large sample sizes [33], [34]. Kendall rank correlation coefficient τ measures correlation between two variables, while the Spearman rank correlation coefficient ρ assesses their monotonic relationship [35], [36]. Squared Euclidean distance d^2 measures the squared distance between each Copula function and the empirical Copula function [37]. Log-likelihood $\log\delta(\theta,u,v)$ evaluates the model's ability to fit observed data pairs (u,v), where u and v are the transformed marginal distributions of wind and PV outputs, respectively [38]. These complementary indicators together ensure a comprehensive and objective selection of the optimal Copula model.

$$\mathrm{AIC} = 2r - 2\ln(\delta) \tag{4}$$

$$\mathrm{BIC} = \ln(n)r - 2\ln(\delta) \tag{5}$$

$$\tau = \frac{2(\zeta_1 - \zeta_2)}{N(N-1)} \tag{6}$$

$$\rho = \frac{\sum_{i=1}^{N}(c_i - \bar{c})(d_i - \bar{d})}{\sqrt{\sum_{i=1}^{N}(c_i - \bar{c})^2}\sqrt{\sum_{i=1}^{N}(d_i - \bar{d})^2}} \tag{7}$$

$$\bar{c} = \frac{\sum_{i=1}^{N} c_i}{N} \tag{8}$$

$$\bar{d} = \frac{\sum_{i=1}^{N} d_i}{N} \tag{9}$$

$$C_n(u_i, v_i) = \frac{1}{n}\sum_{i=1}^{n} I_{[F_n(x_i)\le u]} I_{[F_n(y_i)\le v]} \tag{10}$$

$$d^2 = \sum_{i=1}^{n}\left|C_n(u_i, v_i) - C_{\mathrm{Copula}}(u_i, v_i)\right|^2 \tag{11}$$

$$\log\delta(\theta,u,v) = \sum_{i=1}^{n}\log c_\theta(u_i, v_i) \tag{12}$$

where r is the number of model parameters, δ is the maximum likelihood estimation result, ζ_1 is the number of consistent sample pairs, ζ_2 is the number of inconsistent sample pairs, N is the number of sampling points, c_i is the rank of u_i in $(u_1,u_2,\cdots,u_n)$, d_i is the rank of v_i in $(v_1,v_2,\cdots,v_n)$, $C_n(u_i,v_i)$ and $C_{\mathrm{Copula}}(u_i,v_i)$ are empirical and theoretical Copula functions, respectively, x_i and y_i represent sample values of PV and wind power output, respectively, $F_n(x_i)$ and $F_n(y_i)$ are empirical cumulative distribution functions, θ is the parameter vector, and $c_\theta(u_i,v_i)$ is the Copula density function.

The accuracy of the generated scenarios is evaluated using two statistical metrics: average relative error (ARE) and Kolmogorov–Smirnov (K–S) distance [39], [40].

The ARE metric evaluates the deviation of the generated scenario's mean value from the original dataset, and is defined as:

$$\mathrm{ARE} = \frac{1}{2}\sum_{i=1}^{2}\left|\frac{\mu_i^{\mathrm{gen}} - \mu_i^{\mathrm{orig}}}{\mu_i^{\mathrm{orig}}}\right| \tag{13}$$

where μ_i^{gen} and μ_i^{orig} denote the average values of the i-th resource type in the generated scenarios and the original dataset, respectively.

The K–S distance $D_{n,n}$ measures the maximum discrepancy between the empirical cumulative distribution functions of the generated and original datasets:

$$D_{n,n} = \sup_x\left|F_n(x) - F_n^{'}(x)\right| \tag{14}$$

where $F_n^{'}(x)$ and $F_n(x)$ represent the empirical distribution functions of the original and generated samples, respectively.

C. Decision-making Model

When selecting a Copula function, various evaluation indicators and evaluation methods may yield different results. To achieve optimal performance, we combine one subjective and two objective decision-making approaches to ensure a more balanced and accurate evaluation.

For this reason, we propose an integrated decision model for GRA that combines subjective triangular fuzzy analytic hierarchy process (TF-AHP) with objective entropy weighting (EWM) and criteria importance through inter-criteria correlation (CRITIC) methods. This combined approach is particularly effective for selecting representative daily wind power and PV output data, improving the reliability of scheduling research.

1) TF-AHP

TF-AHP is a subjective weighting method that uses triangular fuzzy numbers to capture subjectivity and uncertainty in pairwise comparisons. Fuzzy comprehensive evaluation offers a rigorous and streamlined method to simplify and quantify multi-criteria dataset scoring [41]. The hierarchical structure is illustrated in Fig. 2.

$$r_{i_0} = \frac{\sum_{j_0=1}^{n} q_{i_0 j_0}}{\sum_{k_0=1}^{n}\sum_{j_0=1}^{n} q_{k_0 j_0}}, i_0 = 1,2,\cdots,n \tag{15}$$

where r_{i_0} is the weight of the i_0-th indicator, $q_{i_0 j_0}$ and $q_{k_0 j_0}$ are entries in i_0-th and k_0-th row individually of column j_0 in the evaluation matrix, respectively, and n is the total number of indicators.

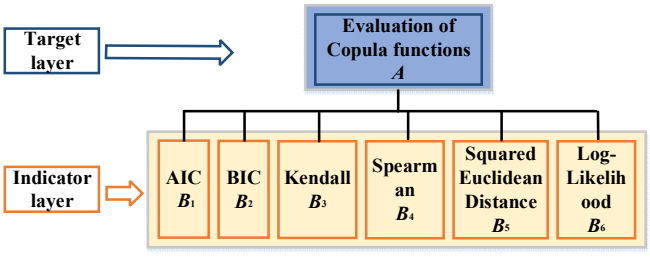


Fig. 2. The hierarchical structure of dataset assessment.

2) CRITIC

CRITIC is an objective weighting method that evaluates contrast by each indicator's standard deviation (higher deviations indicate a wider range of values) and conflict by inter-indicator correlations (stronger positive correlations denote lower conflict) [42].

Firstly, the original indicator values are forward-oriented and standardized to form matrix $b'_{i_0 j_0}$.

$$b'_{i_0 j_0} = \begin{cases} \dfrac{x^{\max}(j_0) - x_{i_0}(j_0)}{x^{\max}(j_0) - x^{\min}(j_0)}, \text{if indicator } j_0 \text{ is negative} \\ \dfrac{x_{i_0}(j_0) - x^{\min}(j_0)}{x^{\max}(j_0) - x^{\min}(j_0)}, \text{if indicator } j_0 \text{ is positive} \end{cases} \tag{16}$$

where $x_{i_0}(j_0)$ is the original value of indicator j_0, and $x^{\max}(j_0)$ and $x^{\min}(j_0)$ are maximum and minimum values of that indicator.

Secondly, calculate each indicator's information capacity.

$$\sigma_{j_0} = \sqrt{\frac{\sum_{i_0=1}^{m} (b'_{i_0 j_0} - \bar{x}_{j_0})}{m-1}} \tag{17}$$

$$f_{j_0} = \sum_{i_0=1}^{m} (1 - r_{i_0 j_0}) \tag{18}$$

$$C_{j_0} = \sigma_{j_0} f_{j_0} \tag{19}$$

where $\bar{x}_{j_0}$ is the mean of indicator j_0, $r_{i_0 j_0}$ is the correlation coefficient between indicators i_0 and j_0, m is the number of samples, C_{j_0} is the information capacity, σ_{j_0} is the contrast, and f_{j_0} is the conflict.

Finally, calculate the weight ω_{j_0} of each indicator.

$$\omega_{j_0} = \frac{C_{j_0}}{\sum_{k_0=1}^{n} C_{k_0}}, j_0 = 1, 2, \cdots, n \tag{20}$$

3) EWM

EWM objectively weights indicators by their variability. Indicators with lower entropy convey more information and thus receive higher weights, whereas those with higher entropy convey less information and receive lower weights [43].

Firstly, calculate the probability matrix P_{j_0} for each indicator.

$$P_{j_0} = \frac{b'_{i_0 j_0}}{\sum_{i_0=1}^{m} b'_{i_0 j_0}} \tag{21}$$

Secondly, calculate each indicator's information entropy e_{j_0} and corresponding utility value d_{j_0}.

$$e_{j_0} = -\frac{1}{\ln m} \sum_{i_0=1}^{m} b'_{i_0 j_0} \ln b'_{i_0 j_0} \tag{22}$$

$$d_{j_0} = 1 - e_{j_0} \tag{23}$$

Finally, calculate the weight W_{j_0} of each indicator.

$$W_{j_0} = \frac{d_{j_0}}{\sum_{k_0=1}^{n} d_{k_0}}, j_0 = 1, 2, \cdots, n \tag{24}$$

4) GRA

GRA applies geometric measures to quantify each dataset's proximity to an ideal value, and smaller deviations indicate stronger alignment [44].

Compute the mean of the processed array x, derive each index's correlation coefficient, and then calculate the grey correlation degree. The formulas are given as follows:

$$x'_{i_0}(j_0) = \frac{x_{i_0}(j_0)}{\bar{x}'_{j_0}} \tag{25}$$

$$\zeta_{i_0}(j_0) = \frac{\Delta_{\min} + \rho \Delta_{\max}}{\Delta_{i_0}(j_0) + \rho \Delta_{\max}} \tag{26}$$

$$D = \frac{1}{m} \sum_{j_0=1}^{n} \zeta_{i_0}(j_0) \tag{27}$$

where $\zeta_{i_0}(j_0)$ is the correlation coefficient of the j_0-th indicator, $x'_{i_0}(j_0)$ denotes the j_0-th indicator value of the ideal Copula, formed by the optimal values of all evaluation metrics, $\bar{x}'_{j_0}$ is the average value, $\Delta_{i_0}(j_0) = \left| x'_0(j_0) - x'_{i_0}(j_0) \right|$, $\Delta_{\max} = \max_{i_0} \max_{j_0} \Delta_{i_0}(j_0)$, $\Delta_{\min} = \min_{i_0} \min_{j_0} \Delta_{i_0}(j_0)$, and ρ is the resolution coefficient, generally taken as 0.5.

5) Improved GRA

To capture the multifaceted impact of indicators on dataset stability, GRA combines TF–AHP, CRITIC, and EWM for an objective, holistic evaluation of each dataset. This framework optimizes model selection, as shown in Fig. 3.

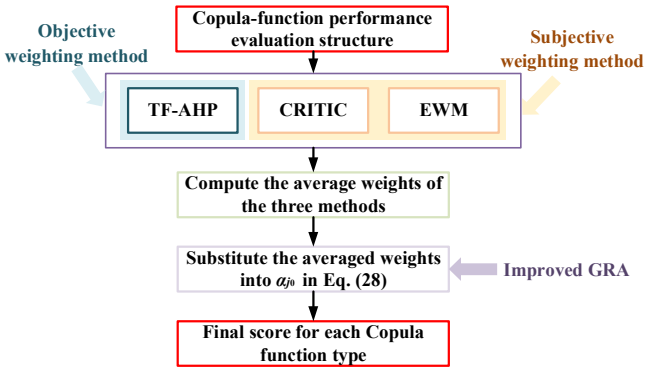


Fig. 3. Evaluation flowchart for each dataset.

Indicator weights from these models are averaged to obtain α_{j_0}. Eq. 27 is updated to the following grey relational formula:

$$D_0 = \sum_{j_0=1}^{n} \alpha_{j_0} \zeta_{i_0}(j_0) \tag{28}$$

D. User Allocation Mechanism

User allocation in overlapping coverage areas is crucial because associating users with different BSs can lead to varying power consumption. Optimizing the user allocation helps minimize the overall power consumption of BSs. This approach is crucial for determining the BSES backup capacity and enabling its participation in scheduling. The power consumption of a 5G BS in double modes is given in Eq. 29 [45].

$$P_{i,t}^{5G} = \begin{cases} P_{i,t}^{static} + \beta P_{i,t}^{active}, S_{i,t} = 1 \\ P_{i,t}^{sleep}, S_{i,t} = 0 \end{cases} \tag{29}$$

$$P_{i,t}^{active} = N_0(2^{\frac{L_j}{B}} - 1)\cdot 10^{\frac{A_{pl}\lg(d_{i,j})+B_{pl}}{10}} \tag{30}$$

$$L_j = a_0 + a_1 \sin(\frac{\pi t}{12} + \varphi_1) + a_2 \sin(\frac{\pi t}{6} + \varphi_2) \tag{31}$$

where i and j represent the indices of BSs and users, respectively, $S_{i,t} = 1$ and $S_{i,t} = 0$ represent the BS in active and sleep states respectively, $P_{i,t}^{static}$ is the fixed power consumption in the working state, necessary for the BS to maintain normal operation, $P_{i,t}^{active}$ is the dynamic power consumption, β denotes the energy efficiency factor, $P_{i,t}^{sleep}$ is the power consumption in the sleep state, N_0 is the channel white noise, B is the channel bandwidth, L_j is the user traffic demand, A_{pl} and B_{pl} are the channel fading coefficients, $d_{i,j}$ is the distance between the user and the BS, a_0, a_1, a_2 are the coefficients of communication flow, φ_1 and ψ_2 are phases. Adjusting these parameters allows for generating communication flow expressions for different areas.

Optimizing 5G BSs' dynamic power consumption is key for EMSs and affects backup ES capacity. The objective function is given as follows:

$$\min \sum_{t=1}^{24} \sum_{i=1}^{n} P_{i,t}^{5G} \tag{32}$$

The optimization model should incorporate the following communication restrictions so as to satisfy QoS criteria.

1) Connection constraints.

$$\sum_{i \in I_j} Z_{i,j,t} = 1 \tag{33}$$

$$Z_{i,j,t} \le S_{i,t}, i \in I_j \tag{34}$$

where $Z_{i,j,t}$ is the connection relationship between BS i and user j at time t, $Z_{i,j,t} = 1$ means connected, $Z_{i,j,t} = 0$ means disconnected, $S_{i,t}$ is the working status variable of the BS, and I_j is the set of BSs to which the user can connect at this moment. Eq. (33) ensures that each user is associated with only one BS at any given time. Eq. (34) guarantees that the connection is established only with an active BS.

2) Transmission flow constraints.

$$L_{i,t} = \sum_{j \in N_i} Z_{i,j,t} L \tag{35}$$

$$L_{i,t} \le L_{\max} \tag{36}$$

where $L_{i,t}$ represents the traffic of BS i at that moment, L is the traffic demand of a single user, N_i is the set of users covered by BS i, and $L_{\max}$ is the upper limit of the traffic.

3) BS transmit power constraints.

$$P_{i,t}^{tr} \le P_{\max}^{tr} \tag{37}$$

where $P_{i,t}^{tr}$ is the transmit power of BS i, and $P_{\max}^{tr}$ represents the maximum transmit power.

4) BS bandwidth constraints.

$$B_{i,t} = \sum_{j \in N_i} Z_{i,j,t} B \tag{38}$$

$$B_{i,t} \le B_{\max} \tag{39}$$

where $B_{i,t}$ is the bandwidth of BS i, B is the bandwidth requirement of a single user, and $B_{\max}$ is the upper limit of the BS bandwidth.

5) Constraints on user's QoS.

$$R_{i,j,t} \ge R_{i,j,t}^{req} Z_{i,j,t} \tag{40}$$

where $R_{i,j,t}^{req}$ is the transmission rate that satisfies the user's QoS at time t.

According to Shannon's theorem, the transmission rate is determined by the bandwidth B allocated to the user and the signal to interference plus noise ratio (SINR).

$$R_{i,j,t} = B\log(1 + \mathrm{SINR}_{i,j,t}) \tag{41}$$

$$\mathrm{SINR}_{i,j,t} = \frac{P_{i,j,t}^{tr} g_{i,j}}{N_0 + \sum_{i' \in N, i' \ne i} P_{i',j,t}^{tr} g_{i',j}} \tag{42}$$

$$g_{i,j} = \begin{cases} A(\frac{d_{i,j}}{d_0})^{-\alpha}, d_{i,j} \ge d_0 \\ A, \quad 0 \le d_{i,j} \le d_0 \end{cases} \tag{43}$$

where $P_{i,j,t}^{tr}$ is the transmission power corresponding to BS i connecting to user j, $g_{i,j}$ is the channel gain, d_0 is the reference distance, A is the fixed path loss, and α is the path-loss exponent.

E. BSES Backup Capacity

ES serves as a backup power source for 5G BSs during distribution failure. The BSES power capacity in this study is split into two portions: the backup capacity to ensure reliability during emergencies and the dispatchable capacity that can engage in grid interactions to improve economic efficiency [46]. Optimizing BSES backup configuration while increasing dispatchable capacity can improve sustainability and network efficiency.

Traditional ES devices have a fixed output range, but backup ES for 5G BSs is variable due to temporal and spatial volatility. This study assesses backup ES considering grid node vulnerability, load levels, and BS power consumption.

$$X_i^{backup}(t) = \frac{V_k}{\sum_{k=1}^{n} V_k} \cdot \int_t^{t+T_i^{backup}} P_{i,t}^{5G} dt \tag{44}$$

$$T_i^{backup} = (\frac{d_k}{d_1 + d_2 + d_3})^{-1} \cdot T_0 \tag{45}$$

where T_i^{backup} is the ES backup time, V_k is the vulnerability at the node k, d_k is the load level, T_0 is the minimum backup time, and $X_i^{backup}(t)$ is the backup ES capacity.

Eq. (44) defines the relationship between the backup capacity and the main influencing factors. The backup capacity is proportional to both the BS's power consumption and the vulnerability of the grid node. A higher node vulnerability V_k indicates weaker grid support and therefore leads to a larger capacity allocation to enhance reliability. Consequently, BSs

located at more vulnerable nodes or with higher power demand receive greater backup capacity, ensuring sufficient emergency supply. Here, the vulnerability index is not used to classify nodes into categories such as critical or normal. Instead, it is treated as a continuous measure of relative node vulnerability for differentiated BSES backup capacity allocation.

Eq. (45) provides a heuristic definition of variable backup time. The parameters d_1, d_2, d_3 are dimensionless coefficients representing three load levels, representing Grade 1 (most critical), Grade 2, and Grade 3 (least critical). The reciprocal form ensures that a higher load grade (smaller d_k) yields a longer backup duration. This ensures that critical BSs retain power supply for longer periods, while less critical ones rely on shorter backup durations.

Configuring BSES capacity requires a framework for assessing the vulnerability of power network nodes. In real cascading failure processes, the vulnerability of a node may be affected by failures in neighboring nodes due to topology reconfiguration, power flow redistribution, and possible islanding. However, such dynamic post-fault behavior lies beyond the scope of this study. Therefore, the following methods are adopted to evaluate the static potential vulnerability of nodes under the given network configuration.

1) Topology-based methods [47].

- Degree centrality

$$M_D(k) = o_k \tag{46}$$

where o_k is the degree of node k, that is, the number of edges directly connected to node k.

- Closeness centrality

$$C_C(k) = \frac{1}{\sum_{k'=1}^{n} d(k,k')} \tag{47}$$

where $d(k,k')$ is the shortest path distance from node k to node k', and n is the number of nodes connected to node k.

- Betweenness centrality

$$M_B(k) = \sum_{k \neq k' \neq k''} \frac{\sigma_{k'k''}(k)}{\sigma_{k'k''}} \tag{48}$$

where $\sigma_{k'k''}$ is the total number of shortest paths between node k' and node k'', and $\sigma_{k'k''}(k)$ is the total number of shortest paths between node k' and node k'' passing through node k.

2) Electrical parameters-based methods.

- Voltage stability index (VSI) [48]

$$\mathrm{VSI}_{kk'} = \frac{4 \cdot (V_k \cdot V_k')}{Q_k' \cdot X_{kk'}} \tag{49}$$

where V_k and V_k' are the voltage amplitudes, Q_k' is the reactive power demand at node k', and $X_{kk'}$ is the reactance.

- Power flow sensitivity [49]

The Jacobian matrix elements are calculated as follows:

When $k = k'$

$$\begin{cases} J_{11}(k,k) = -Q_k - V_k^2 \cdot \mathrm{Im}(Y_{bus}(k,k)) \\ J_{12}(k,k) = -P_k + V_k^2 \cdot \mathrm{Re}(Y_{bus}(k,k)) \\ J_{21}(k,k) = P_k - V_k^2 \cdot \mathrm{Re}(Y_{bus}(k,k)) \\ J_{22}(k,k) = Q_k - V_k^2 \cdot \mathrm{Im}(Y_{bus}(k,k)) \end{cases} \tag{50}$$

When $k \neq k'$

$$\begin{cases} J_{11}(k,k') = V_k V_k' \left[E \sin(\theta_k - \theta_k') - F \cos(\theta_k - \theta_k') \right] \\ J_{12}(k,k') = V_k V_k' [E \cos(\theta_k - \theta_k') + F \sin(\theta_k - \theta_k')] \\ J_{21}(k,k') = V_k V_k' [E \cos(\theta_k - \theta_k') + F \cos(\theta_k - \theta_k')] \\ J_{22}(k,k') = V_k V_k' [E \sin(\theta_k - \theta_k') - F \cos(\theta_k - \theta_k')] \end{cases} \tag{51}$$

where $J_{11}, J_{12}, J_{21}, J_{22}$ denote the four sub-blocks of the Jacobian matrix, corresponding to partial derivatives of power injections with respect to voltage magnitudes and angles, P_k and Q_k are the active and reactive power injections at node k, $Y_{bus}(k,k')$ is the (k,k') -th element of the bus admittance matrix, θ_k and θ_k' are voltage phase angles, $E = \mathrm{Re}(Y_{bus}(k,k'))$, and $F = \mathrm{Im}(Y_{bus}(k,k'))$.

The sensitivity matrix is obtained from the inverse J^{-1} of each sub-matrix:

$$\left(\frac{\partial \theta}{\partial P'}, \frac{\partial \theta}{\partial Q'}, \frac{\partial V}{\partial P'}, \frac{\partial V}{\partial Q'}\right) = J^{-1} \tag{52}$$

where P' and Q' denote small perturbations in active and reactive power injections, while θ and V represent the system responses in voltage phase angles and magnitudes, respectively. This matrix captures how voltage states respond to changes in power injections.

The sensitivity matrices are averaged with equal weights to obtain the comprehensive power flow sensitivity matrix:

$$\text{average_sensitivity} = \frac{1}{4}\left(\frac{\partial \theta}{\partial P'} + \frac{\partial \theta}{\partial Q'} + \frac{\partial V}{\partial P'} + \frac{\partial V}{\partial Q'}\right) \tag{53}$$

To quantify the influence of each node on the power flow distribution, the sensitivity values across all other nodes are aggregated. Specifically, for each node k, the row sum of the sensitivity matrix is used to represent its overall power flow sensitivity:

$$\text{node_sensitivity}(k) = \sum_{k' \neq k} \text{average_sensitivity}(k,k') \tag{54}$$

- Short-circuit current [50]

$$I_{sc,k} = \left| \frac{V_k}{Z_{th,k}} \right| \tag{55}$$

where $Z_{th,k}$ is the Thevenin equivalent impedance.

- Network efficiency [51]

$$H = \frac{1}{N(N-1)} \sum_{k \neq k'} \frac{1}{d(k,k')} \tag{56}$$

$$H_k = \frac{1}{(N-1)(N-2)} \sum_{k \neq k', k' \neq k'', k \neq k''} \frac{1}{d_{k'k''}^{(k)}} \tag{57}$$

$$\Delta H_k = \left| H - H_k \right| \tag{58}$$

where H is the initial network efficiency, H_k is the efficiency after removing node k, $d_{k'k''}^{(k)}$ is the shortest path between k' and k'' without node k, and ΔH_k is the efficiency loss.

3) Statistical methods.

The voltage Theil entropy is a statistical indicator used to measure the degree of voltage distribution imbalance and the sensitivity of each node to power fluctuations. It quantifies how the voltage deviation across nodes changes with incremental power injections, thereby reflecting the vulnerability of nodes to voltage instability. A higher Theil entropy value indicates a less uniform voltage response and thus a more fragile network structure [52], [53].

- Voltage Theil entropy

$$Y_{kk'} = \left| \frac{U_{kk'} - U_0}{U_0 - U_{cr}} \right| \tag{59}$$

$$Y_k = \sum_{k'=1}^{N} Y_{kk'} \tag{60}$$

$$T_{taier}(k) = \sum_{k'=1}^{N} \frac{Y_{kk'}}{Y_k} [\log(\frac{Y_{kk'} / Y_k}{N_k / N}) + \log(\frac{Y_{kk'} / Y_k}{1/N})] \tag{61}$$

where U_0 is the initial voltage of each node obtained by power flow calculation, U_{cr} is the critical voltage value, $U_{kk'}$ is the new voltage value after adding unit active power to each node k, $Y_{kk'}$ is the voltage crossing probability, Y_k is the voltage change influence coefficient, and $T_{taier}(k)$ is voltage Theil entropy.

The voltage Theil entropy is computed using the base-case power-flow state and the voltage responses to unit active-power injection perturbations, rather than relying on long-term high-resolution time-series data. As such, it captures static node vulnerability under the specific operating condition under study, without explicitly accounting for seasonal variations in renewable energy within this index.

The Gini coefficient is introduced to evaluate the overall structural imbalance of the distribution network from a topological perspective. It measures the inequality of node connectivity and betweenness, indicating whether certain nodes dominate the network's structural importance. A larger Gini coefficient implies a more uneven network structure, where failures in critical nodes could have a greater impact on system stability [54].

- Gini coefficient

$$\rho_n = \alpha_1 \left(\frac{1}{N} \|D\|_1 \right) + \alpha_2 \|D\|_\infty \tag{62}$$

$$R_D(k) = \frac{M_D(k) - \bar{M}_D}{\bar{M}_D} \tag{63}$$

$$R_B(i) = \frac{M_B(i) - \bar{M}_B}{\bar{M}_B} \tag{64}$$

$$G = 1 - 2\sum_{k=1}^{N} \frac{M_k}{N} \tag{65}$$

$$G(k) = \rho_n \cdot R_D(k) \cdot G_D \cdot R_B(k) \cdot G_B \tag{66}$$

where $\|D\|_1$ is the 1-norm of the node degree set, representing the sum of all node degrees, $\|D\|_\infty$ is the infinity norm of the node degree set, representing the maximum value among the node degrees, ρ_n is the weighted average node degree, α_1 and α_2 are weight factors, N is the total number of nodes, $R_D(k)$ is the degree influence rate, $R_B(k)$ is the betweenness influence rate, $\bar{M}_D$ is the average value of node degree, $\bar{M}_B$ is the average value of node betweenness, G is the original Gini coefficient, $G(k)$ is the modified Gini coefficient, G_D and G_B are the Gini coefficients of degree and betweenness, respectively, and M_k is the k-th value of the Lorenz curve.

IV. Scheduling Modeling

Analyzing the dispatch and operation of 5G BSMGs enables more efficient energy allocation across time periods. A day-ahead scheduling model is formulated to minimize the operating cost while maximizing the renewable-energy utilization. The operating cost represents the total electricity expense of the BSMG system, calculated from grid energy purchases and the operating states of BSs and ES units. Both sub-objectives are normalized to remove dimensional differences: the cost term is inversely normalized, and the utilization term is positively normalized. To ensure consistency, the normalization bounds are defined at the hourly scale, representing the theoretical upper and lower limits of hourly operating cost and renewable energy utilization. The cost bounds are estimated from the highest and lowest grid prices combined with the system load range, while the utilization bounds correspond to full and zero use of available renewable generation. These bounds remain constant for all hourly periods within the 24-hour scheduling horizon, and the objective aggregates the normalized hourly values over the entire horizon, forming a mixed-integer linear programming (MILP) problem solved by CPLEX. The objective function is as follows:

$$\max \sum_{t=1}^{24} (\omega_1 \lambda'_{normolized}(t) + \omega_2 \lambda_{normolized}(t)) \tag{67}$$

$$\lambda'_{normalized}(t) = \frac{\lambda'^{\max}_{net} - \lambda'_{net}}{\lambda'^{\max}_{net} - \lambda'^{\min}_{net}} \tag{68}$$

$$\lambda_{normolized}(t) = \frac{\lambda - \lambda^{\min}}{\lambda^{\max} - \lambda^{\min}} \tag{69}$$

where $\lambda'_{normalized}(t)$ is the normalized 5G BSMGs operating cost, $\lambda_{normolized}(t)$ is the normalized wind and PV power consumption rate, ω_1 and ω_2 are the weights of the two sub-objectives, set to 0.5 to equally balance 5G BSMG operating cost and renewable energy utilization, $\lambda'^{\max}_{net}$ and $\lambda'^{\min}_{net}$ represent the maximum and minimum values of BSMGs operating costs, respectively, $\lambda^{\max}$ and $\lambda^{\min}$ denote the maximum and minimum values of wind and PV power consumption rates, respectively, λ'_{net} and λ are the operating cost and renewable energy utilization rate, respectively.

$$\lambda_{net}^{'} = \lambda_{grid}^{'} + \lambda_{ES}^{'} \tag{70}$$

$$\lambda_{grid}^{'} = \sum_{t=1}^{24} \pi_t P_t^{grid} \tag{71}$$

$$\lambda_{ES}^{'} = \sum_{t=1}^{24} \lambda_{bat}^{'} \cdot (P_{t,dis} / \eta + P_{t,ch}\eta) \tag{72}$$

$$\lambda = \sum_{t=1}^{24} \begin{cases} \dfrac{P_{load}(t) + P_{t,ch}}{P_{pv}(t) + P_{pw}(t)}, & P_{load}(t) + P_{t,ch} \le P_{pv}(t) + P_{pw}(t) \\ 1, & P_{load}(t) + P_{t,ch} > P_{pv}(t) + P_{pw}(t) \end{cases} \tag{73}$$

where $\lambda_{grid}^{'}$ is the grid exchange cost, and $\lambda_{ES}^{'}$ denotes the BSES operation cost. π_t is the time-of-use electricity price, and P_t^{grid} is the grid exchange power between 5G BSMGs and the distribution network. $\lambda_{bat}^{'}$ represents the BSES charging and discharging cost, while $P_{t,dis}$ and $P_{t,ch}$ are the BSES discharge and charging power, respectively. η is the charging and discharging efficiency, $P_{load}(t)$ is the load, $P_{pv}(t)$ is the PV output, and $P_{pw}(t)$ is the wind power output.

1) Inequality constraints.

$$0 \le P_{t,dis} \le P_{t,dis}^{\max} \tag{74}$$

$$0 \le P_{t,ch} \le P_{t,ch}^{\max} \tag{75}$$

$$E_{BS}^{\min} \le E_s(0) + \eta \sum_{t=1}^{T} [P_{t,ch}\Delta t] - \frac{1}{\eta} \sum_{t=1}^{T} [P_{t,dis}\Delta t] \le E_{BS}^{\max} \tag{76}$$

$$E_{BS}^{\min} \le E_s(t) \le E_{BS}^{\max} \tag{77}$$

$$S_{t,dis} + S_{t,ch} \le 1 \tag{78}$$

where T is the scheduling period, a $P_{t,ch}^{\max}$ and $P_{t,dis}^{\max}$ are the maximum charging and discharging power, $E_s(0)$ is the initial BSES capacity, $E_{BS}^{\max}$ and $E_{BS}^{\min}$ are its maximum and minimum allowable capacities during scheduling, $E_s(t)$ is the BSES capacity at time t, $S_{t,dis}$ and $S_{t,ch}$ are binary variables representing the BSES operating state. Eq. (78) ensures that the ES cannot charge and discharge simultaneously, while allowing both states to reach zero when the system is idle.

2) Equality constraints.

$$\eta \sum_{t=1}^{T} [P_{t,ch}\Delta t] - \frac{1}{\eta} \sum_{t=1}^{T} [P_{t,dis}\Delta t] = 0 \tag{79}$$

$$E_s(t+1) = E_s(t) + \eta P_{t,ch}\Delta t - \frac{1}{\eta} P_{t,dis}\Delta t \tag{80}$$

$$P_t^{grid} = P_L(t) + P_{t,ch} - P_{pv}(t) - P_{pw}(t) - P_{t,dis} \tag{81}$$

where $E_s(t+1)$ is the BSES capacity at time t+1. Eq. (79) maintains capacity consistency, enabling cyclic scheduling. Eq. (80) describes the time-coupled SoC evolution, ensuring that the battery capacity remains within limits at each time step.

V. Case Study

To verify the effectiveness of the proposed approach, extensive studies are implemented in MATLAB using the CPLEX solver on a computer equipped with an Intel Core i7-13700H CPU (2.40 GHz, 13th Gen) and 32 GB RAM. The simulations are conducted on the IEEE 33-bus system to optimize BSES capacity, evaluate node vulnerability, and reduce operating costs, ensuring both practical applicability and computational efficiency.

A. Data Preparation

The dataset used in this study consists of hourly wind and PV power output data obtained from the Fingrid Open Data Portal (https://data.fingrid.fi/en/datasets). The data cover the period from 1 January 2023 to 31 December 2023, comprising a full year of 8,760 hourly samples. It includes real power measurements in kilowatts with a resolution of one hour, covering seasonal and daily variations across the year.

The raw Fingrid data is adapted to the studied microgrids' installed capacities using a two-step normalization and scaling process. First, the wind and PV power time series are normalized by their maximum observed values, and then the normalized series are scaled according to predefined capacity limits. This normalization-and-scaling approach retains the original temporal characteristics and cross-correlation of renewable generation, while maintaining consistency with the capacity assumptions used in the optimization model.

To illustrate representative temporal characteristics without overcrowding the figures, Fig. 4 presents one-week wind and PV output samples for four representative seasons. Specifically, Fig. 4(a) illustrates the spring profile, where PV output begins to rise and wind generation exhibits frequent fluctuations. Fig. 4(b) shows the summer profile, characterized by relatively higher and more concentrated PV output during daytime hours. Fig. 4(c) depicts the fall profile, in which PV output declines relative to summer while wind generation remains highly variable. Fig. 4(d) presents the winter profile, featuring lower PV output and more dominant wind generation, particularly at night. These seasonal differences and the complementary behavior between wind and PV generation further motivate the use of a Copula-based approach to model their joint variability.

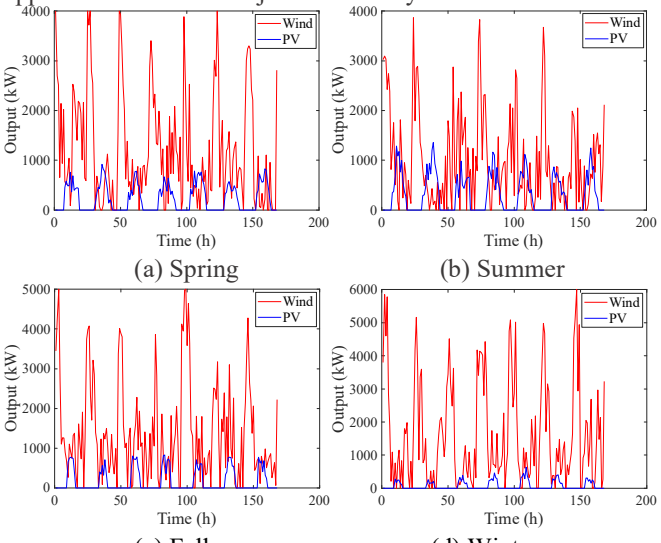


Fig. 4. One-week wind and PV power output profiles for four representative seasons: (a) spring, (b) summer, (c) fall, and (d) winter.

B. Typical Scenario Generation of Wind and PV Output

Six evaluation metrics have been assessed on the RES outputs derived from full-year data sample reduction using the Copula functions to select representative scenarios, as shown in Table III. It is shown that Clayton excels in AIC, Kendall, and Spearman but underperforms in the other 3 indicators, making it difficult to identify the best Copula function.

TABLE III
CALCULATION RESULTS OF COPULA FUNCTION INDICATORS

Type	AIC	BIC	Kendall	Spearman	d^2	Log-Likelihood
Normal	-281	-94	-0.11	-0.15	3.33	189
t	-414	-227	-0.13	-0.18	5.4	255
Gumbel	84	272	-0.05	-0.07	1.3	5.8
Clayton	25	162	-0.05	-0.07	7.3	61
Frank	-259	-72	-0.12	-0.17	11.8	177

The relative scores of the five Copula functions, calculated using Eq. (28) and the indicator average weights shown in Fig. 5, based on future RES outputs derived from full-year data sample reduction, are 0.752, 0.722, 0.619, 0.602, and 0.777. With the highest score of 0.777, the Frank-Copula is selected.

Using this fitted Copula, a large number of synthetic scenarios are generated to represent the probabilistic behavior of renewable energy outputs. A scenario reduction method based on K-means clustering is applied to extract five representative scenarios from each data segment: spring (March–May), summer (June–August), fall (September–November), winter (December–February), and the whole year. These reduced scenarios are directly derived from the original data in each corresponding period, and their occurrence probabilities are determined according to the cluster proportions. The resulting representative RES generation profiles serve as inputs for the subsequent scheduling optimization, effectively capturing seasonal variability while maintaining computational tractability.

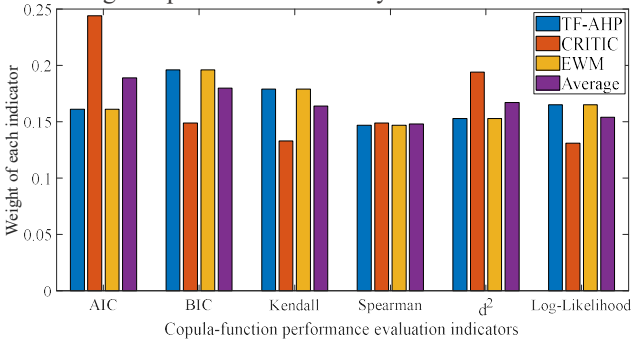
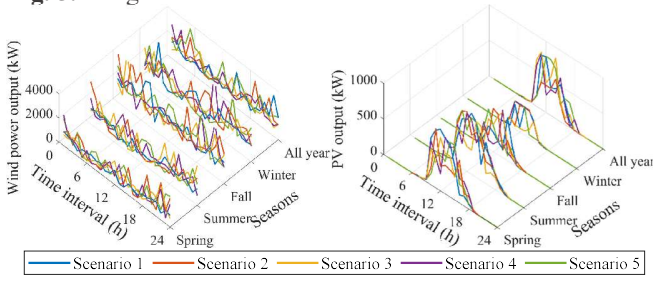


Fig. 5. Weight results of each indicator.



(a) Wind power (b) PV

Fig. 6. Five representative renewable generation scenarios selected via Copula-based scenario reduction for RES outputs across different seasons and the full year.

As shown in Fig. 6, the selected scenarios retain the key temporal patterns of the original data. Each color in Fig. 6 corresponds to one of the five representative output scenarios obtained after scenario reduction for each season and for the whole-year dataset. Among the five Copula functions, Frank-Copula achieves the highest weighted score of 0.777 and is therefore selected. To validate the effectiveness of the Frank Copula in generating synthetic renewable energy scenarios, statistical tests are conducted. As shown in Table IV, the proposed Copula achieves the lowest ARE and K–S distance among all candidates. Specifically, the ARE is below 5% and the K–S distance is approximately 0.06, indicating that the selected Copula not only ranks highest in accuracy but also ensures reliable and distribution-consistent scenario generation.

TABLE IV
COMPARISON OF DIFFERENT COPULA FUNCTIONS

Copula	ARE	K-S
Normal	0.046	0.079
t	0.051	0.082
Gumbel	0.057	0.094
Clayton	0.065	0.103
Frank (Proposed)	0.039	0.061

As shown in Table V, the sensitivity analysis indicates that the Frank Copula consistently achieves the highest score across all weighting scenarios. When TF-AHP judgments varied by ±10% or indicator weights were perturbed by ±20%, the score only fluctuated slightly (0.773–0.789) but the ranking remained unchanged. Even when subjective weights were excluded, the Frank Copula still ranked first, confirming the robustness of the proposed evaluation framework.

TABLE V
SENSITIVITY ANALYSIS OF COPULA-FUNCTION EVALUATION

Scenario	Normal	*t*	Gumbel	Clayton	Frank
Vary TF-AHP pairwise judgments (±10%)	0.745	0.739	0.617	0.599	0.773
Exclude TF-AHP weights	0.498	0.477	0.418	0.406	0.512
Perturb all indicator weights (±20%)	0.764	0.734	0.622	0.607	0.789

Following Copula-based scenario reduction, five representative renewable generation scenarios are retained per season and for the annual case. The reduction process assigns a probability weight to each retained scenario, thereby approximating the original stochastic distribution of renewable uncertainty. These scenario–probability pairs are incorporated into the optimization model by evaluating scheduling decisions across all representative scenarios and weighting the corresponding operational costs by their assigned probabilities.

C. User Allocation Mechanism and BS Power Consumption

To evaluate the performance of the distribution network under realistic load conditions, this study models both residential and office areas based on node locations and assumed usage types. Residential loads are characterized by demand peaks in the early morning and evening hours, reflecting typical household activity patterns, while office

loads exhibit peak consumption during standard working hours. The load profiles for all nodes are generated using the BS power model described in Eqs. (29)-(31), where in the power demand is driven by time-varying user traffic and the operational states of BSs, as depicted in Fig. 7. Load priority levels are assigned according to the criticality of the corresponding services, with priority categories indicated by color codes in Fig. 8. Based on this setup, the IEEE 33-bus distribution system is employed for simulation, with a base voltage of 12.66 kV. Two PV units rated at 500 kW are integrated at nodes 16 and 20, while two wind power generation units rated at 2,000 kW are connected at nodes 24 and 28.

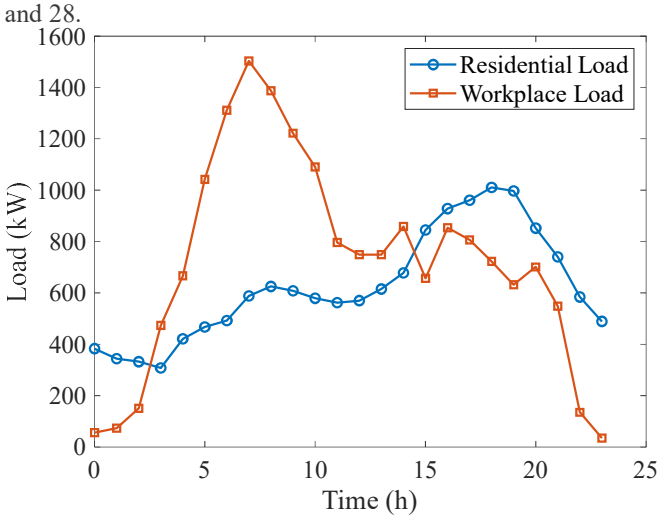


Fig. 7. Typical daily load profiles for residential and work place areas.

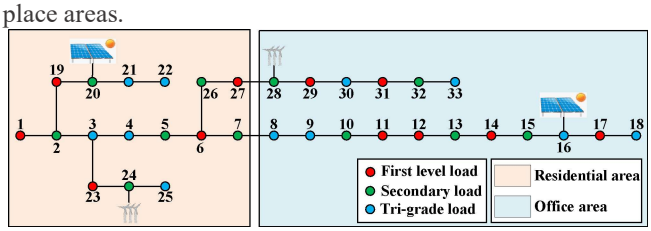


Fig. 8. IEEE 33-node bus system.

Following the methodology in [52] and the 5G planning framework proposed in [55], this study determines the number and locations of BSs through a two-step approach. In the first stage, the optimal number of BSs is obtained by solving a multi-objective problem that balances coverage, redundancy, and deployment cost, with equal importance assigned to the three factors [55]. In the second stage, K-means clustering is applied to the IEEE 33-bus node coordinates to determine the spatial layout of BSs, where the optimized BS number serves as the number of clusters. All features are normalized to [0,1] using min–max scaling to ensure equal weighting, and the K-means++ initialization strategy is adopted to enhance clustering stability. Each clustering process is repeated multiple times with random seeds, and the configuration yielding the minimum within-cluster variance is selected. The centroid of each cluster is selected as a BS deployment site, ensuring that BSs are spatially distributed in accordance with the underlying network topology. Based on the clustering results and node distances, the system is partitioned into 18 areas, with a total of 124 BSs deployed accordingly, the number of nodes and BSs assigned to each area is summarized in Table VI. Unlike [52], this study does not incorporate node importance metrics derived from energy or information flow. Instead, the clustering is guided purely by spatial proximity and the structural characteristics of the distribution network. To simulate realistic traffic conditions, 10,000 users are randomly generated following a Poisson distribution, representing spatial and temporal variability in user demand. These users are associated with the nearest BSs within each cluster. The communication parameters used in the simulation are provided in Table VII [13].

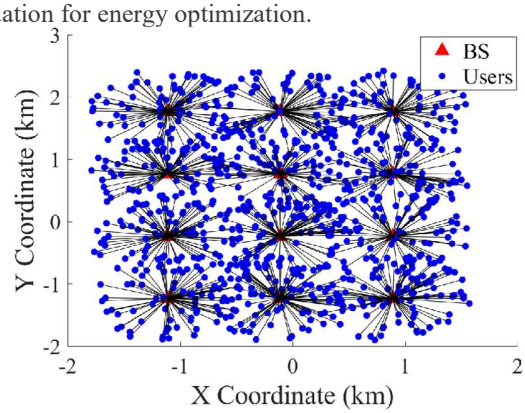
TABLE VI
COMPARISON OF DIFFERENT COPULA FUNCTIONS

Region	Node	BS	Region	Node	BS
1	1, 2, 19	1-12	10	10	81-86
2	20	12-24	11	11	87-90
3	3, 23	25-36	12	12, 13	91-94
4	24, 25	37-48	13	14, 15	95-106
5	4, 21, 22	49-60	14	16	107, 108
6	5	61-66	15	17	109-112
7	6, 7	67-72	16	18	113
8	8	73, 74	17	26	114, 115
9	9	75-80	18	27-33	116-124

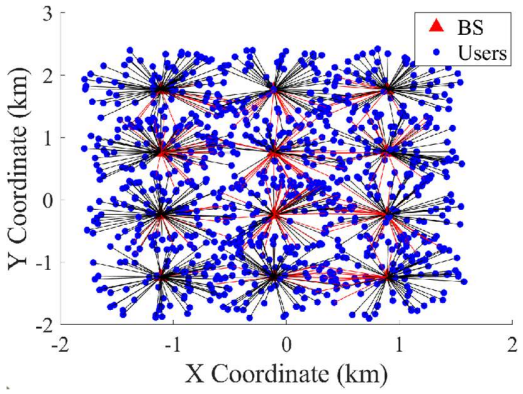
TABLE VII
COMMUNICATION PARAMETER SETTINGS

Parameter	Value	Parameter	Value
$P_{i,t}^{static}$ (kW)	2.3	$B_{\max}$ (Mhz)	100
$P_{i,t}^{sleep}$ (kW)	1.5	$P_{\max}^{tr}$ (W)	550
β	2.8571	$L_{\max}$ (Mbit/s)	10^4
BS coverage radius (km)	0.7	A (dB)	-35
A_{pl}	37.6	α	2.5
B_{pl}	128.1	d_0 (m)	1
User data rate (Mbit/s)	[50,100]		

Fig. 9 illustrates the user-to-BS association and migration patterns in the first region across two consecutive hours. In each hour, user associations are updated based on the system state, allowing users to dynamically switch serving BSs. Black lines represent users whose serving BSs remain unchanged, while red lines indicate users that have migrated to different BSs in the subsequent hour. This dynamic reassignment mechanism enables flexible load balancing and prepares the foundation for energy optimization.



(a) Hour 1



(b) Hour 2

Fig. 9. Spatial distribution of user–BS association and migration at different time instants.

Fig. 10 illustrates the hourly number of users served by the 12 BSs in region 1 (line graph) and the changes in user numbers between consecutive hours (bar graph). Generally, user changes per hour are fewer than 20. Centrally located BSs 6 and 7, having the most neighboring BSs, experience the largest fluctuations in user numbers, indicating that greater coverage overlapping leads to higher user variability. In contrast, peripheral BSs 1, 4, 9, and 12, having fewer neighboring BSs, show minimal fluctuations.

This study compares three user-to-BS association strategies for evaluating system performance and BS power efficiency: the power-prioritized method, the distance-prioritized method, and the load-balancing method. These methods differ in how users are assigned to BSs and how BS activity is managed throughout the day. Table VIII compares the number of users served by each BS under these three methods in area 1.

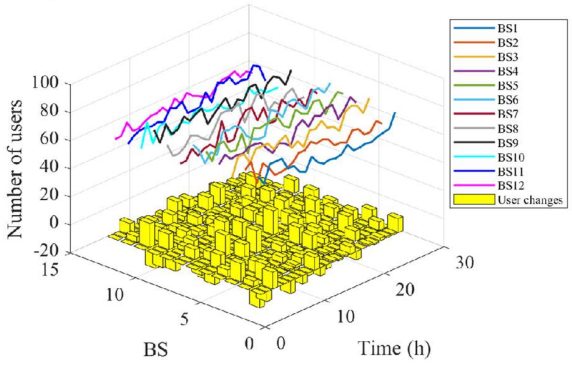


Fig. 10. Hourly variation in the number of users served by different BSs in area 1 over a 24-hour period.

TABLE VIII
NUMBER OF USERS IN REGION 1

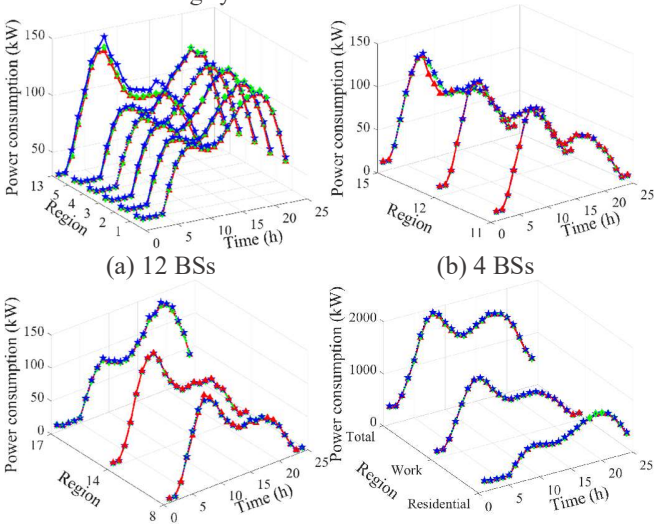
BS	Number of users		
	Power	Distance	Load balance
1	70-87	66	67
2	70-87	69	71
3	73-87	86	83
4	70-86	81	82
5	71-87	85	85
6	70-87	91	81
7	70-87	72	79
8	70-87	77	78
9	74-87	84	84
10	70-87	67	70
11	70-86	83	81
12	70-80	78	78

Power-Prioritized Method: This is the method proposed in this study. It aims to minimize total BS power consumption by dynamically optimizing user-to-BS associations within each time slot, subject to BS coverage constraints. Rather than turning BSs on or off, the method focuses on reallocating users in overlapping coverage areas to BSs that can serve them at a lower power cost, according to the BS power model and real-time traffic demand. For users located in non-overlapping regions, their serving BSs remain fixed. As traffic patterns change over time, user associations are adaptively adjusted to improve overall energy efficiency without violating connectivity requirements [56].

Distance-Prioritized Method: In this method, each user is connected to the geographically nearest BS. This minimizes path loss and generally improves received signal strength. However, because the assignment is purely distance-based, some BSs may become overloaded while others are underutilized, leading to imbalanced resource usage [57].

Load-Balancing Method: This method assigns users to BSs with the lightest current load, aiming to evenly distribute traffic across all BSs. While it helps avoid BS overloads and promotes fairness in resource usage, it may increase the average connection distance for some users, which can degrade signal quality and increase transmission power [58].

Fig. 11 compares the power consumption differences across various regions under different user-BS association strategies. Although these curves appear to be similar, they clearly show the overall temporal trends of BS power consumption under different methods. The quantitative differences between the strategies are further quantified in Table VII for clearer comparison. As shown in Fig. 11(a), (b), and (c), when the number of BSs exceeds four, the power-prioritized method consistently outperforms both the distance-prioritized and load-balancing methods in terms of energy efficiency. As the number of BSs decreases, the performance gap narrows, indicating reduced optimization flexibility. Fig. 11(d) illustrates the tidal effect between residential and work areas, where distinct temporal load patterns are observed. This further supports the effectiveness of separate scheduling in matching supply with demand, thereby minimizing energy waste and reducing system costs.



(a) 12 BSs (b) 4 BSs

(c) 2 BSs (d) Work and residential region

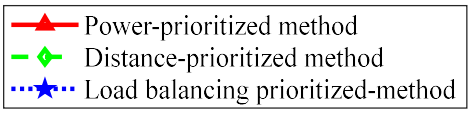


Fig. 11. Comparison of power consumption in different regions.

Table IX reports the range of energy consumption differences between the proposed power-prioritized method and two baseline strategies. Positive values indicate that the baseline method consumed more energy. As shown in Table IX, the total power consumption difference reaches up to 18.455 kW·h for the distance-prioritized method and 25.922 kW·h for the load balancing method. These values correspond to a 3.691% and 5.184% reduction in total energy consumption, respectively, clearly demonstrating the overall energy-saving advantage of the proposed strategy.

TABLE IX
COMPARISON OF BS ENERGY CONSUMPTION DIFFERENCES (BASELINE – PROPOSED METHOD)

Number of BSs	Region	Difference (Distance-Proposed) (kW·h)	Difference (Load balancing-Proposed) (kW·h)
12	1	[0.042, 3.423]	[0.607, 4.403]
	2	[0.049, 3.209]	[0.673, 4.287]
	3	[0.033, 2.416]	[0.656, 5.391]
	4	[0.018, 2.035]	[0.574, 5.115]
	5	[0.028, 2.565]	[0.592, 5.330]
	13	[0.034, 3.018]	[0.649, 12.423]
4	11	[-0.957, -0.079]	[-0.896, 0.640]
	12	[-1.028, -0.009]	[-0.777, 1.765]
	15	[-3.878, 12.833]	[-2.210, 15.185]
2	8	[-0.215, 1.281]	[-0.332, 0.981]
	14	[-0.910, -0.713]	[-0.271, -0.054]
	17	[0, 0.049]	[0, 4.871]
Type	Work	[0.352, 17.148]	[5.233, 18.882]
	Residential	[0.721, 14.286]	[1.342, 20.771]
	Total	[1.211, 18.455]	[3.761, 19.455]

To further assess the effectiveness of the proposed user–BS association strategies, a baseline with BS sleep-mode control is added. In this scheme, a BS switches to sleep when its load falls below a threshold and all served users can be reassigned to neighboring active BSs without violating coverage or capacity constraints.

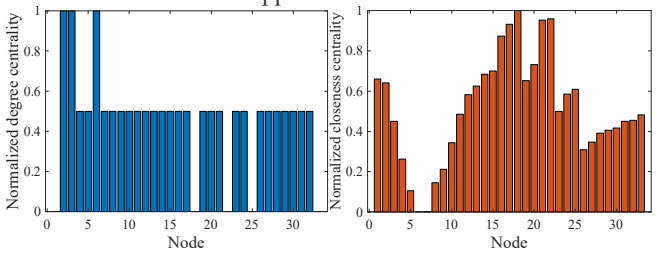
Table X summarizes the 24-hour average BS power consumption of the three association methods with and without sleep mode. The enabling sleep mode provides additional energy savings across all strategies, with the largest reduction (2.699%) achieved by the power-prioritized method. This method naturally aggregates users to energy-efficient BSs, leaving more neighboring BSs lightly loaded and eligible for deactivation. In contrast, the distance- and load-balancing methods distribute users more evenly across BSs, resulting in fewer idle cells and smaller additional savings (1.336% and 0.963%, respectively).

TABLE X
AVERAGE BS POWER CONSUMPTION WITH AND WITHOUT SLEEP MODE IN TOTAL REGION

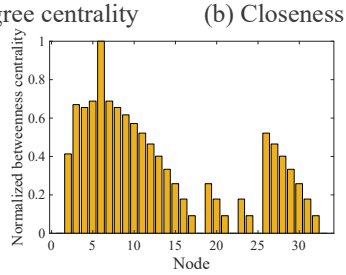
Association Strategy	Without sleep mode (kW·h)	With sleep mode (kW·h)	Additional saving (%)
Power-prioritized	1237.5	1204.1	2.699
Distance-prioritized	1250.4	1233.7	1.336
Load-balancing	1256.7	1244.6	0.963

D. BSES Backup Capacity

The node vulnerability results obtained from topological, electrical, and statistical-based methods are illustrated in Figs. 12-14, respectively, while the comprehensive evaluation results are shown in Fig. 15. Each single-method vulnerability assessment results in zero values for certain nodes, which is unrealistic in practical terms. Moreover, indicators such as short-circuit current and network efficiency tend to produce overall higher vulnerability scores, while corresponding Gini coefficients are relatively low. These inconsistencies highlight the limitations of relying on individual metrics and demonstrate the need for a more comprehensive, multi-dimensional evaluation approach.

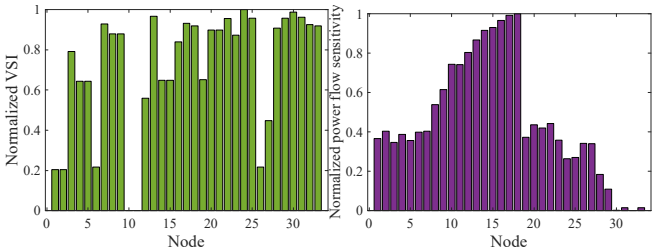


(a) Degree centrality (b) Closeness centrality

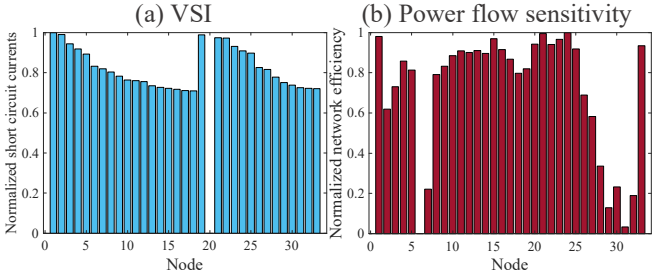


(c) Betweenness centrality

Fig. 12. Node vulnerability based on topological structure method.



(a) VSI (b) Power flow sensitivity

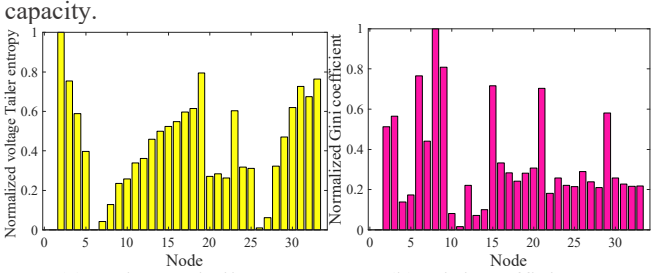


(c) Short circuit current (d) Network efficiency

Fig. 13. Node vulnerability based on electrical parameters method.

Fig. 16(a) shows the BSES backup time at each node. Nodes 1, 2, 7, 10, 12, 17, 19, 24, 28, and 32 have the longest BSES backup time of 6 hours, while nodes 3, 5, 14, 20, 23, 25, and 30 have 3 hours. The remaining nodes have the shortest backup time of 2 hours. Fig. 16(b) shows the BSES backup

capacity in 18 locations at various times using the power-prioritized user allocation approach. It can be seen that regions 1, 12, and 17 have the largest backup capacities, while other areas have roughly half of their capacity. The dispatchable ES is calculated as the BSES rated capacity minus the backup capacity.



(a) Voltage Theil entropy (b) Gini coefficient

Fig. 14. Node vulnerability based on statistical and entropy method.

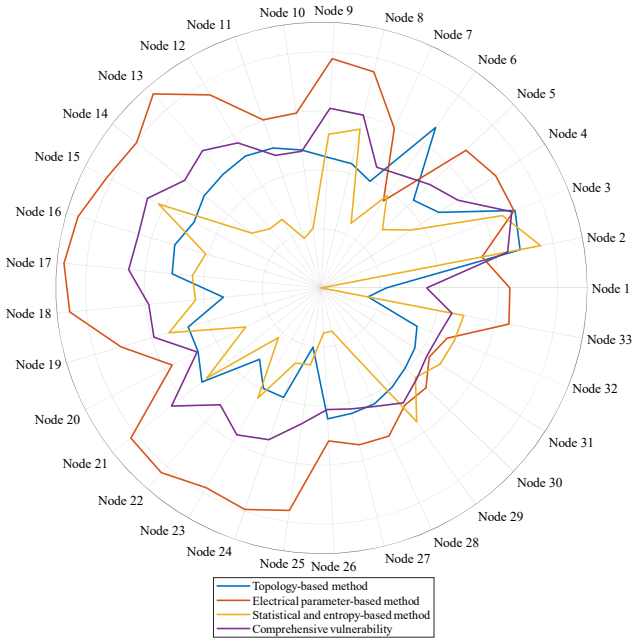
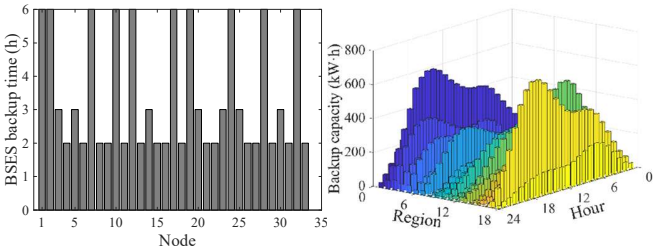


Fig. 15. Comparison of different node vulnerability assessment methods.



(a) Time (b) Capacity

Fig. 16. BSES backup configuration.

Table XI compares BSES dispatchable capacities. The power-prioritized method requires the least backup capacity, followed by the distance-prioritized method, while the load-balancing method requires the most, potentially raising costs.

TABLE XI
BSES CAPACITY BY ALLOCATION METHOD

Type	Power	Distance	Load balance
Backup, Residential (kW·h)	298	652	661
Dispatchable, Residential (kW·h)	1382	1028	1019
Backup, Work (kW·h)	196	430	435
Dispatchable, Work (kW·h)	804	570	565

Fig. 17 shows the ES backup capacity calculated by different vulnerability assessment methods for node 1. Some individual vulnerability assessment methods such as degree centrality, betweenness centrality, voltage Theil entropy, and the Gini coefficient assign zero vulnerability to certain nodes, resulting in a calculated backup capacity of zero. This outcome is clearly unrealistic and highlights a significant limitation of these methods. In contrast, methods based on short circuit currents and network efficiency tend to overestimate node vulnerability, leading to excessively high backup capacity. The VSI method tends to underestimate vulnerability, resulting in unreasonably low-capacity values. These findings demonstrate that relying on a single metric can lead to overly extreme or biased results.

Compared with other representative methods, the proposed strategy achieves consistent reductions in the required backup capacity range. To ensure a fair comparison, we excluded methods with zero backup capacity (e.g., Gini coefficient, Voltage Theil entropy), those with extremely low upper bounds (e.g., VSI), and methods with abnormally high estimates (e.g., short circuit currents). As shown in Table XII, and based on the remaining practical and representative methods, the lower bound of the required capacity is reduced by 0.57–16.77 kW·h, equivalent to 2.8%–45.9%, while the upper bound is reduced by 4.80–291.17 kW·h, corresponding to 2.8%–63.6%. This indicates that the proposed method not only reduces the peak backup requirement but also narrows the overall capacity range. By avoiding both over-sizing and under-sizing issues, it enhances the dispatchability and resource efficiency of ES systems.

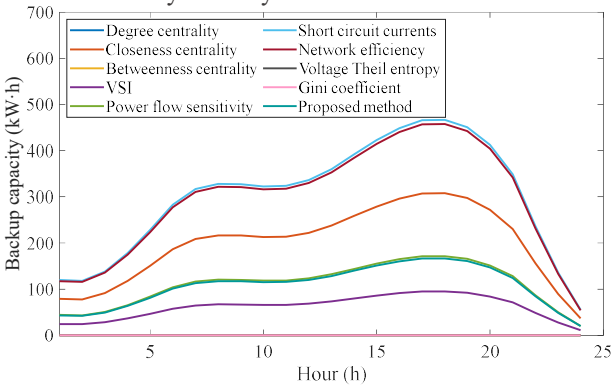


Fig. 17. Impact of node vulnerability assessment methods on backup capacity.

TABLE XII
BACKUP CAPACITY BY VULNERABILITY ASSESSMENT METHOD

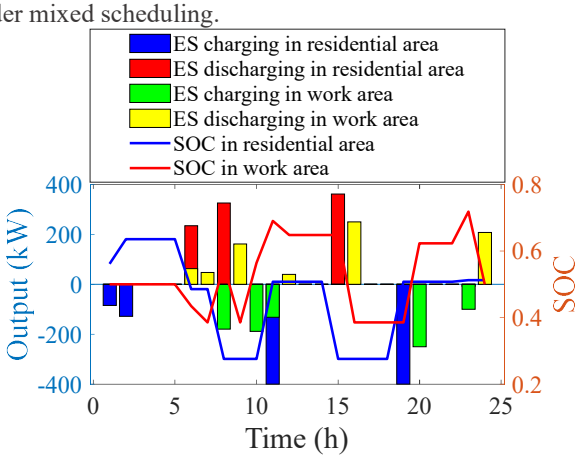
Method	Capacity range (kW·h)
Degree centrality	0
Closeness centrality	[36.53, 307.83]
Betweenness centrality	0
VSI	[11.29, 95.16]
Power flow sensitivity	[20.33, 171.32]
Short circuit currents	[55.38, 466.7]
Network efficiency	[54.31, 457.69]
Voltage Theil entropy	0
Gini coefficient	0
Proposed method	[19.76, 166.52]

E. Scheduling Results

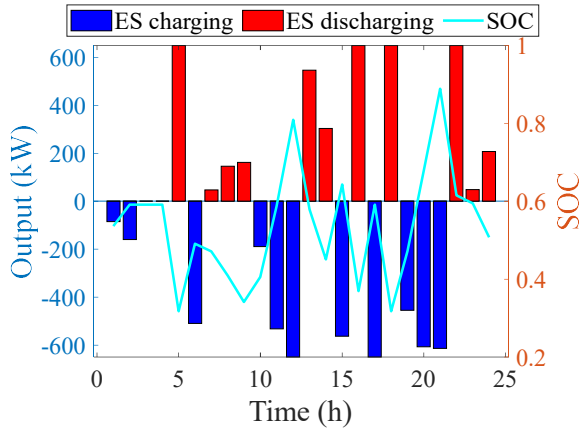
The electricity prices utilized for cost computation and energy trading evaluation are extracted from the Nord Pool day-ahead electricity market (https://data.nordpoolgroup.com/auction/day-ahead/prices). These hourly spot prices follow the official settlement convention and are initially denominated in EUR/MW·h. To maintain consistency with the USD-denominated economic metrics used in this study, the prices are uniformly converted to USD using a fixed average exchange rate across all scheduling strategies compared.

This study evaluates the operational performance of mixed and separate scheduling methods. In the mixed scheduling approach, the residential and office areas are treated as a single integrated region, with unified optimization of ES operation and grid power exchange. However, the two areas exhibit distinct load profiles, residential demand typically peaks in the early morning and evening, while office demand is concentrated during the day. This discrepancy can lead to inefficient resource allocation, reduced scheduling flexibility, and higher operating costs. In contrast, the separate scheduling strategy manages the residential and office areas independently, allowing each to optimize storage dispatch and grid interaction based on its own demand and renewable generation. This localized control better matches area-specific load variations, improves the utilization of storage resources, enhances adaptability to renewable fluctuations, and reduces overall costs.

In this study, five independent scenario-reduction processes are conducted based on the Copula-generated RES data, corresponding to spring, summer, fall, winter, and the entire year. Among these studies, the year-wide reduction results are used as the inputs to the scheduling as shown in Fig. 18 and Fig. 19 which represent the overall annual operation. Specifically, Fig. 18 illustrates the BSES output and SOC variations under regional and hybrid scheduling. In Fig. 18(a), discharging occurs mainly in the morning, afternoon, and midnight, with charging peaks at midday, evening, and early morning. Work areas show frequent daytime charging and discharging, while residential areas concentrate these at night. Fig. 18(b) highlights more intensive charging and discharging under mixed scheduling.



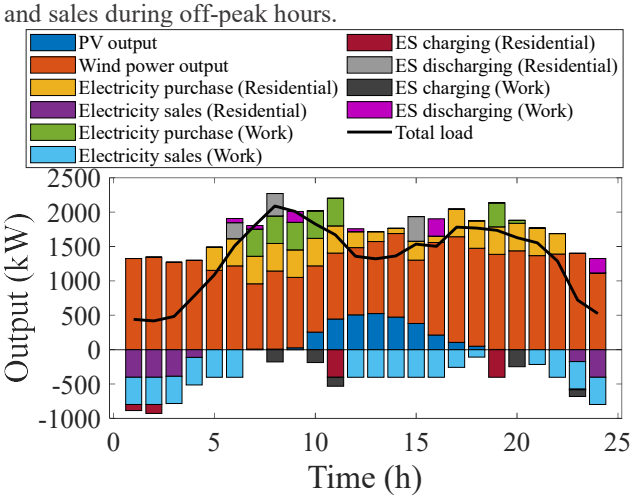
(a) Separate scheduling



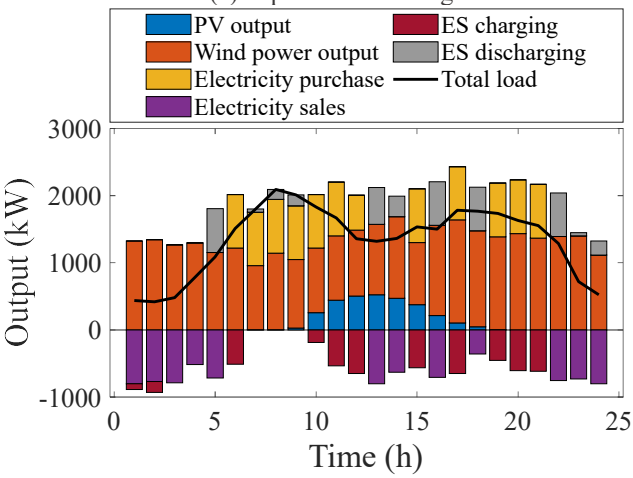
(b) Merge scheduling

Fig. 18. The output of BSES in different areas.

Fig. 19 shows power output variations based on the same year-wide typical-day scenarios used in Fig. 18. In Fig. 19(a), work area electricity sales occur in the evening, early morning, and afternoon, while residential sales peak in the early morning. Purchases focus on the morning in work areas and are more dispersed in residential areas. Fig. 19(b) shows that mixed scheduling concentrates purchases during peak daytime and sales during off-peak hours.



(a) Separate scheduling



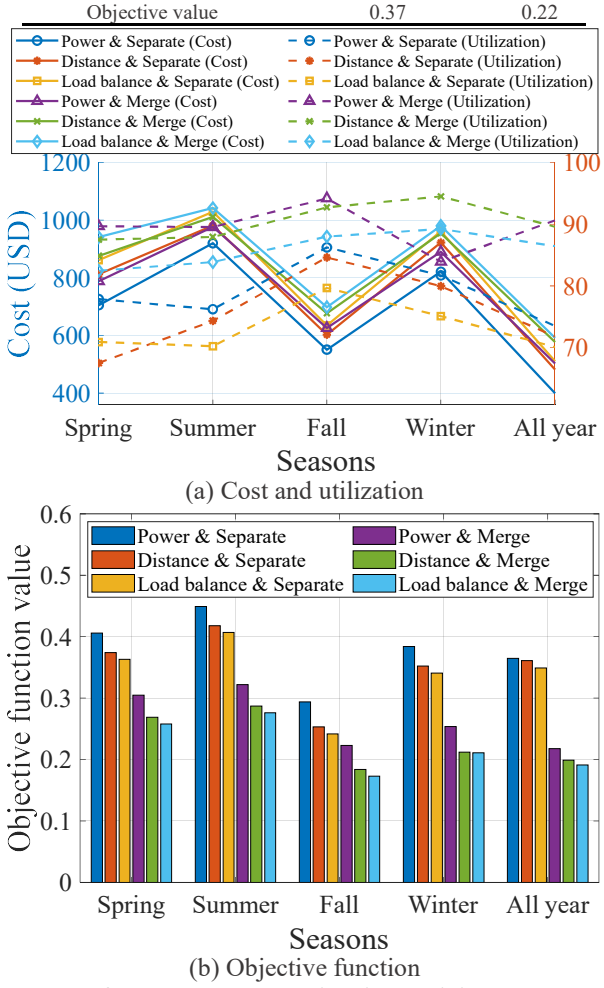
(b) Merge scheduling

Fig. 19. System power balance diagram in different areas.

Wind and PV power outputs are generated through scenario reduction using Copula-based joint probabilistic modeling of annual renewable profiles. Compared with the mixed scheduling strategy, the separate scheduling approach results in lower electricity purchases, reduced energy trading volumes, and less battery cycling. Notably, it increases renewable energy utilization by 3.5%, reduces operating cost by $101 (a 20.1% decrease), and improves the overall objective function value by 0.15, representing a 68.2% enhancement. These comparative results are summarized in Table XIII, highlighting the superior economic and energy performance of applying separate scheduling to residential and work areas.

TABLE XIII
COMPARISON OF SCHEDULING RESULTS

Parameter	Separate		Merge
	Residential	Work	
Purchase electricity (kW·h)	5849	2388	9313
Sold electricity (kW·h)	1875	6183	8363
ES charging (kW·h)	1020	851	5013
ES discharging (kW·h)	851	768	4061
Operating cost ($)	401		502
Renewable energy utilization (%)	76	79	74
Objective value	0.37		0.22



(a) Cost and utilization

(b) Objective function

Fig. 20. Performance on seasonal and annual datasets.

Fig. 20 compares the performance of the proposed methods across five datasets derived from typical days representing four seasons and the entire year. As shown in Fig. 20(a), separate scheduling achieves lower operation costs and higher renewable energy utilization than mixed scheduling, with power-prioritized methods performing best. Fig. 20(b) shows separate scheduling has higher objective function values, while power-prioritized methods slightly outperform others within each scheduling type. Given the hourly scheduling framework, the extent of cost reduction fluctuates on an hourly basis. Fig. 20 demonstrates that, when aggregated across typical daily, seasonal, and annual scenarios, the proposed method consistently yields overall performance improvements.

F. Computational Complexity and Scalability

To evaluate the computational tractability of the proposed optimization model, the IEEE 33-bus distribution network was partitioned into 18 spatial regions according to the node and BS clustering results shown in Table VI. Each region is optimized independently using the proposed BS–user association and power scheduling framework, while the boundary consistency is maintained across adjacent areas. This partition-based approach significantly reduces the number of binary decision variables and improves scalability without noticeable loss of optimality.

Among 18 regions, 17 of which contain multiple BSs and are actively optimized, whereas the smallest region (with a single BS) requires no association optimization since all users are directly served by that BS. The user population across the 17 optimized regions ranges from 173 to 1047, with an average of approximately 540 users. For each region, let r_1 denote the number of users, r_2 is the number of BSs, and r_3 is the number of candidate BSs per user ($r_3 \leqslant r_2$). In the complexity estimation, $r_3 \approx r_2$ is adopted as the worst-case assumption, where all BSs are considered potential candidates for each user. Considering BS coverage limits, the actual computational scale is typically lower. For the hourly optimization, the model includes $r_1 r_3$ binary variables and about $2r_1 r_3 + r_2$ continuous variables (for BS transmit power, bandwidth, user data rate, and SINR). In the smallest active region (r_1=173, r_2=2), this corresponds to roughly 346 binary and 700 continuous variables, and converges within 10 minutes. In contrast, the largest region (r_1=1047, r_2=12) expands to around 1.3×10^4 binary and 2.5×10^4 continuous variables, requiring up to 45 minutes to reach convergence. Across all optimized regions, the average solving time per hourly MILP problem is approximately 25–30 minutes when the CPLEX is used to solve the optimization problem in combination with MATLAB, and the number of linear constraints scales to several thousand per region due to the coupling of the communication and power networks in the problem formulation.

The computation time scales approximately linearly with the number of users and BSs in each region, confirming the efficiency of the partition-based formulation. These results demonstrate that the proposed framework effectively balances the solution accuracy and computational burden, and remains scalable for large-scale 5G–based energy management scenarios.

G. Further Discussions

The results presented in Section V confirm the superiorities of the proposed 5G-based BSMG optimization framework.

1) Uncertainty-aware renewable modeling: The Copula-based scenario generation approach effectively captures the stochastic and temporal characteristics of wind and PV power outputs. By comparing five Copula families using the improved GRA method, the most suitable dependence structure is selected, ensuring that realistic and representative renewable generation scenarios are used for subsequent scheduling optimization.

2) Power-saving user–BS association: The proposed time–space–QoS-constrained user association strategy dynamically reallocates users among neighboring BSs according to real-time load and renewable availability. This adaptive mechanism minimizes total BS power consumption while maintaining stable network performance and service reliability.

3) Enhanced dispatchable energy storage: With reduced BS energy demand, the required backup capacity of BSESs is significantly lowered. As a result, a larger portion of the storage becomes dispatchable, improving system flexibility and enabling active participation in energy trading and peak regulation.

4) Multi-objective scheduling optimization: The partitioned scheduling model jointly minimizes operating cost and maximizes renewable energy utilization. By decoupling work and residential areas, the proposed framework achieves a better trade-off between the cost efficiency and renewable consumption compared with traditional mixed scheduling methods.

Overall, these findings show that integrating uncertainty-aware renewable modeling, adaptive communication–energy coordination, and multi-objective optimization can substantially improve the cost-effectiveness, sustainability, and operational flexibility of 5G-enabled smart microgrids.

VI. CONCLUSION

An improved GRA technique is introduced to evaluate multiple Copula functions, selecting the optimal one for scenario reduction to obtain representative wind and PV power outputs for scheduling. A spatial-temporal distributed user allocation method is designed to reduce BS power consumption. A variable backup time concept for BSES is proposed, along with a node vulnerability evaluation method that considers topology, electrical parameters, and statistical entropy. This approach enhances dispatchable capacity while meeting backup power requirements. To balance renewable energy utilization and operational cost, an integrated objective function is formulated that simultaneously maximizes wind and PV power absorption while minimizing the operating cost of BSMGs. The proposed methods are validated using the IEEE 33-bus system, leading to the following conclusions:

1) The proposed improved GRA method combines EWM, CRITIC, and TF-AHP to evaluate Copula functions more rationally. It identifies Frank-Copula as the most suitable with a top score of 0.777. Validation shows that the generated scenarios achieve ARE below 5% and K–S distance around 0.06, confirming the accuracy of the selection.

2) Optimizing BS operational modes and user association strategies leads to a total energy consumption reduction of up to 25.92 kW·h, corresponding to a 5.18% decrease compared to the baseline methods. This demonstrates the effectiveness of the proposed approach in enhancing energy efficiency and promoting more sustainable network operations.

3) By integrating multiple vulnerability metrics, the proposed method reduces backup ES capacity by 0.57 kW·h to 291.17 kW·h compared to individual approaches, corresponding to a 2.8%–63.6% reduction, thereby improving accuracy and dispatchable potential. Compared to distance- and load-based methods, the power-prioritized strategy lowers backup demand by 354 and 363 kW·h, respectively, enabling greater ES utilization.

4) Compared to merged scheduling, separate dispatching lowers operating cost by $101, increases renewable energy utilization from 74% to 76–79%, and improves the objective value from 0.22 to 0.37, thereby enhancing energy storage efficiency and overall system performance.

Despite the promising results listed above, several limitations of this study point to future research directions. The current node vulnerability assessment is static and does not account for the dynamic influence of neighboring-node failures during cascading propagation. Future work should incorporate topology reconfiguration, islanding detection, and iterative vulnerability updating to better capture progressive failure scenarios. Additionally, extending the proposed framework to larger, real-world networks and validating it under diverse operating conditions would further demonstrate its scalability and practicality. Finally, integrating machine learning techniques for faster scenario generation and vulnerability assessment could enhance the framework's applicability for real-time BSMG operations.

REFERENCES

[1] B. P. Kumar and U. K. Kommuri, "Review on 5G small cell base station antennas: Design challenges and technologies," *IEEE Access*, vol. 12, pp. 85899–85928, 2024.

[2] R. K. Senapati and P. J. Tanna, "Deep learning-based NOMA system for enhancement of 5G networks: A review," *IEEE Trans. Neural Netw.*, vol. 35, no. 3, pp. 3380–3394, Mar. 2024.

[3] J. Lee, F. Solat, T. Y. Kim, and H. V. Poor, "Federated learning-empowered mobile network management for 5G and beyond networks: From access to core," *IEEE Commun. Surveys Tuts.*, vol. 26, no. 3, pp. 2176–2212, third quarter 2024.

[4] Z. Wang, J. Hu, G. Min, Z. Zhao, Z. Chang, and Z. Wang, "Spatial-temporal cellular traffic prediction for 5G and beyond: A graph neural networks-based approach," *IEEE Trans. Ind. Inform.*, vol. 19, no. 4, pp. 5722–5731, Apr. 2023.

[5] B. Zeng, W. Zhang, P. Hu, J. Sun, and D. Gong, "Synergetic renewable generation allocation and 5G base station placement for decarbonizing development of power distribution system: A multi-objective interval evolutionary optimization approach," *Appl. Energy*, vol. 351, pp. 121831, Dec. 2023.

[6] X. Guan, Z. Xu, Y. Liu, J. Wu, J. Zhu, and W. Xu, "Reduction in energy consumption of the 5G communication system and beyond through collaborative optimization for BS site operation: challenges, efforts and the new approach," *IEEE Trans. Ind. Inform.*, vol. 20, no. 3, pp. 3948–3963, Mar. 2024.

[7] P. Kaur, R. Garg, and V. Kukreja, "Energy-efficiency schemes for base stations in 5G heterogeneous networks: A systematic literature review," *Telecommun. Syst.*, vol. 84, no. 1, pp. 115–151, Sep. 2023.

[8] J. Han, S. Lin, and B. Pu, "Hierarchical energy management of DC microgrid with photovoltaic power generation and energy storage for 5G base station," *Sustainability*, vol. 16, no. 6, pp. 2422, Mar. 2024.

[9] X. Zhang, Z. Wang, H. Liao, Z. Zhou, X. Ma, X. Yin, Z. Wang, Y. Liu, Z. Lu, and G. Lv, "Optimal capacity planning and operation of shared energy storage system for large-scale photovoltaic integrated 5G base stations," *Int. J. Elect. Power Energy Syst.*, vol. 147, pp. 108816, May 2023.

[10] M. Yan, W. Guo, H. Zheng, and T. Qin, "Joint NTP-MAPPO and SDN for energy trading among multi-base-station microgrids," *IEEE Internet Things J.*, Feb. 2024.

[11] P. Yong, N. Zhang, Q. C. Hou, Y. X. Liu, F. Teng, S. Ci, and C. Q. Kang, "Evaluating the dispatchable capacity of base station backup batteries in distribution networks," *IEEE Trans. Smart Grid*, vol. 12, no. 5, pp. 3966–3979, Sep. 2021.

[12] Y. Zou, Q. G. Wang, Y. Chi, J. Wang, C. Lei, N. C. Zhou, and Q. Q. Xia, "Electric load profile of 5G base station in distribution systems based on data flow analysis," *IEEE Trans. Smart Grid*, vol. 13, no. 3, pp. 2452–2466, May 2022.

[13] C. Zhou, C. Feng, and Y. Wang, "Spatial–temporal energy management of base stations in cellular networks," *IEEE Internet Things J.*, vol. 9, no. 13, pp. 10588–10599, 1 Jul. 2022.

[14] X. Ma, Y. Mu, Z. Liu, X. Jiang, J. Zhang, and Y. Gao, "Energy consumption optimization of 5G base stations considering variable threshold sleep mechanism," *Energy Rep.*, vol. 9, pp. 34–42, Aug. 2023.

[15] A. Israr, Q. Yang, and A. Israr, "Renewable microgeneration cooperation with base station sleeping-mode strategy for energy-efficient operation of 5G infrastructures," *Sustain. Energy Grids*, vol. 38, pp. 101358, 2024.

[16] Z. Cai, Y. Tang, W. Guo, T. Chen, H. Zheng, and T. Qin, "Energy management strategy for distributed photovoltaic 5G base station DC microgrid integrated with the CF-P\&O-INC MPPT algorithm," *Energies*, vol. 17, no. 13, pp. 3258, Jul. 2024.

[17] A. Fayad and T. Cinkler, "Energy-efficient joint user and power allocation in 5G millimeter wave networks: a genetic algorithm-based approach," *IEEE Access*, vol. 12, pp. 20019-20030, 2024.

[18] A. Israr, Q. Yang, and A. Israr, "Renewable energy provision and energy-efficient operational management for sustainable 5G infrastructures," *IEEE Trans. Netw. Service Manag.*, vol. 20, no. 3, pp. 2698–2710, Sep. 2023.

[19] M. B. Ali, S. A. A. Kazmi, S. N. Khan, and M. F. Abbas, "Techno-economic assessment and optimization framework with energy storage for hybrid energy resources in base transceiver stations-based infrastructure across various climatic regions at a country scale," *J. Energy Storage*, vol. 72, pp. 108036, Nov. 2023.

[20] Y. Zhou, Q. Wang, Y. Zou, Y. Chi, N. Zhou, X. Zhang, C. Li, and Q. Xia, "Voltage profile optimization of active distribution networks considering dispatchable capacity of 5G base station backup batteries," *J. Mod. Power Syst. Clean Energy*, vol. 11, no. 6, pp. 1842–1856, May 2023.

[21] P. Bao, Q. Xu, and Y. Yang, "Modeling and aggregated control of large-scale 5G base stations and backup energy storage systems towards secondary frequency support," *Appl. Energy*, vol. 357, pp. 122498, Mar. 2024.

[22] P. Yong, N. Zhang, Y. Liu, Q. Hou, Y. Li, and C. Kang, "Exploring the cellular base station dispatch potential towards power system frequency regulation," *IEEE Trans. Power Syst.*, vol. 37, no. 1, pp. 820–823, Jan. 2022.

[23] Y. Dai, C. Li, S. Xia, H. He, P. Wang, and J. Jing, "Collaborative optimization of distribution network and 5G base stations considering its communication load migration and energy storage dynamic backup flexibility," *Int. J. Elect. Power Energy Syst.*, vol. 160, pp. 110124, Sep. 2024.

[24] L. Peng, A. Zhou, J. Qiao, Q. Sun, Z. Qian, M. Xu, and S. Pan, "Day-ahead coordinated scheduling of distribution networks considering 5G base stations and electric vehicles." *Electronics*, vol. 14, no. 19, pp. 3940, 2025.

[25] X. Zhang, Z. Wang, H. Liao, Z. Zhou, X. Ma, X. Yin, Z. Wang, Y. Liu, Z. Lu, and G. Lv, "Optimal capacity planning and operation of shared energy storage system for large-scale photovoltaic integrated 5G base stations," *Int. J. Elect. Power Energy Syst.*, vol. 147, pp. 108816, May 2023.

[26] A. Cabrera-Tobar, F. Grimaccia, and S. Leva, "Energy resilience in telecommunication networks: A comprehensive review of strategies and challenges," *Energies*, vol. 16, no. 18, pp. 6633, Sep. 2023.

[27] Y. Li, T. Chen, Y. She, W. Liao, C. Liu, and M. Xie, "Energy storage regulation strategy for 5G base stations considering power supply reliability," in *Proc. IEEE 7th Conf. Energy Internet Energy Syst. Integr.* (*EI2*), pp. 1573–1578, Dec. 2023.

[28] W. Wu, X. Ji, J. Yang, W. You, B. Xue, D. Zhou, and R. Li, "5G network resilience evaluation mechanism based on Petri nets," *Comput. Netw.*, vol. 257, pp. 110950, Feb. 2025.

[29] G. D. Amico, G. Masala, F. Petroni, and R. A. Sobolewski, "Managing wind power generation via indexed semi-Markov model and copula," *Energies*, vol. 13, no. 16, pp. 4246, Aug. 2020.

[30] X. Ju, X. Liu, S. Liu, and Y. Xiao, "Optimal scheduling of wind–photovoltaic power-generation system based on a copula-based conditional value-at-risk model," *Clean Energy*, vol. 6, no. 4, pp. 550–556, Aug. 2022.

[31] S. Moradian, A. I. Olbert, S. Gharbia, and G. Iglesias, "Copula-based projections of wind power: Ireland as a case study," *Renew. Sustain. Energy Rev.*, vol. 175, pp. 113147, Apr. 2023.

[32] M. S. Smith, "Implicit copulas: An overview," *Econom. Stat.*, vol. 28, pp. 81–104, Oct. 2023.

[33] S. Grønneberg and N. L. Hjort, "The copula information criteria," *Scand. J. Stat.*, vol. 41, no. 2, pp. 436--459, Jun. 2014.

[34] V. Ko, N. L. Hjort, and I. Hobæk Haff, "Focused information criteria for copulas," *Scand. J. Stat.*, vol. 46, no. 4, pp. 1117–1140, Dec. 2019.

[35] H. Z. Muhammed, E. S. A. El-Sherpieny, and E. M. Almetwally, "Dependency measures for new bivariate models based on copula function," *Inf. Sci. Lett.*, vol. 10, no. 3, pp. 511–526, 2021.

[36] I. Gijbels, N. Veraverbeke, and M. Omelka, "Conditional copulas, association measures and their applications," *Comput. Stat. Data Anal.*, vol. 55, no. 5, pp. 1919–1932, May 2011.

[37] Y.-K. Gu, C.-J. Fan, L.-Q. Liang, and J. Zhang, "Reliability calculation method based on the Copula function for mechanical systems with dependent failure," *Ann. Oper. Res.*, pp. 1–18, 2022.

[38] T. Emura and C.-H. Pan, "Parametric likelihood inference and goodness-of-fit for dependently left-truncated data, a copula-based approach," *Statistical Papers*, vol. 61, pp. 479–501, 2020.

[39] H. H. Goh, G. Peng, D. Zhang, W. Dai, T. A. Kurniawan, K. C. Goh, and C. L. Cham, "A new wind speed scenario generation method based on principal component and R-Vine copula theories," *Energies*, vol. 15, no. 7, pp. 2698, Apr. 2022.

[40] T. Lee, R. Modarres, and T. B. M. J. Ouarda, "Data-based analysis of bivariate copula tail dependence for drought duration and severity," *Hydrological Processes*, vol. 27, no. 10, pp. 1454–1463, May 2013.

[41] Y. Liu, C. M. Eckert, and C. Earl, "A review of fuzzy AHP methods for decision-making with subjective judgements," *Expert Syst. Appl.*, vol. 161, pp. 113738, Dec. 2020.

[42] A. M. Hagag, L. S. Yousef, and T. F. Abdelmaguid, "Multi-criteria decision-making for machine selection in manufacturing and construction: recent trends," *Mathematics*, vol. 11, no. 3, pp. 631, 2023.

[43] R. Kumar, S. Singh, P. S. Bilga, J. Singh, S. Singh, M. L. Scutaru, and C. I. Pruncu, "Revealing the benefits of entropy weights method for multi-objective optimization in machining operations: A critical review," *J. Mater. Res. Technol.*, vol. 10, pp. 1471–1492, Jan. 2021.

[44] W. Zhang, X. Zhang, F. Liu, Y. Huang, and Y. Xie, "Evaluation of the urban low-carbon sustainable development capability based on the TOPSIS-BP neural network and grey relational analysis," *Complexity*, vol. 2020, no. 1, pp. 6616988, 2020.

[45] K. C. Chang, K. C. Chu, H. C. Wang, Y. C. Lin, and J. S. Pan, "Energy saving technology of 5G base station based on internet of things collaborative control," *IEEE Access*, vol. 8, pp. 32935–32946, Feb. 2020.

[46] P. Yong, N. Zhang, Q. Hou, Y. Liu, F. Teng, S. Ci, and C. Kang, "Evaluating the dispatchable capacity of base station backup batteries in distribution networks," *IEEE Trans. Smart Grid*, vol. 12, no. 5, pp. 3966–3979, May 2021.

[47] Z. Wang, A. Scaglione, and R. J. Thomas, "Electrical centrality measures for electric power grid vulnerability analysis," *Proc. 49th IEEE Conf. Decis. Control* (*CDC*), pp. 5792–5797, Dec. 2010.

[48] H. S. Salama and I. Vokony, "Voltage stability indices–A comparison and a review," *Comput. Electr. Eng.*, vol. 98, pp. 107743, Mar. 2022.

[49] M. M. Begovic and A. G. Phadke, "Control of voltage stability using sensitivity analysis," *IEEE Trans. Power Syst.*, vol. 7, no. 1, pp. 114–123, Feb. 1992.

[50] P. Chopade and M. Bikdash, "New centrality measures for assessing smart grid vulnerabilities and predicting brownouts and blackouts," *Int. J. Crit. Infrastruct. Prot.*, vol. 12, pp. 29–45, Mar. 2016.

[51]B. Xie, X. Tian, L. Kong, and W. Chen, "The vulnerability of the power grid structure: A system analysis based on complex network theory," *Sensors*, vol. 21, no. 21, pp. 7097, Oct. 2021.
[52]X. Wang, Q. Kang, J. Gao, F. Zhang, X. Wang, X. Qu, and L. Guo, "Distribution network restoration supply method considers 5G base station energy storage participation," Energy, vol. 289, pp. 129825, Feb. 2024.
[53]X. He and W. Fan, "Vulnerability assessment of power system based on Theil entropy of branch potential energy," *Phys. Scr.*, vol. 96, no. 4, pp. 045207, Feb. 2021.
[54]M. Yan, J. Wu, H. Jiang, Y. Kou, and W. Zhao, "Comprehensive vulnerability assessment of power system nodes with wind power based on Dagum-Gini coefficient approach," *Sci. Rep.*, vol. 15, no. 1, pp. 11597, Apr. 2025.
[55]X. Wang, Q. Kang, L. Guo, Z. Liang, J. Gao, and W. Liu, "Economic evaluation for 5G planning of distribution network considering transmission loss and vulnerability," Sustain. Energy Grids Netw., vol. 36, pp. 101231, Dec. 2023.
[56]H. Zhang, S. Huang, C. Jiang, K. Long, V. C. M. Leung, and H. V. Poor, "Energy efficient user association and power allocation in millimeter-wave-based ultra dense networks with energy harvesting base stations," *IEEE J. Sel. Areas Commun.*, vol. 35, no. 9, pp. 1936–1947, Sep. 2017.
[57]K. Son, H. Kim, Y. Yi, and B. Krishnamachari, "Base station operation and user association mechanisms for energy-delay tradeoffs in green cellular networks," *IEEE J. Sel. Areas Commun.*, vol. 29, no. 8, pp. 1525–1536, Aug. 2011.
[58]A. Alizadeh and M. Vu, "Load balancing user association in millimeter wave MIMO networks," *IEEE Trans. Wireless Commun.*, vol. 18, no. 6, pp. 2932–2945, Jun. 2019.



Yingqi Zhu (Student Member, IEEE) received the B.Eng. degree in electrical engineering from North China University of Water Resources and Electric Power, Zhengzhou, China, in 2020, the M.Sc. degree in electrical engineering from University of Shanghai for Science and Technology, Shanghai, China, in 2023. She is currently working toward the Ph.D. degree in electronic and electrical engineering. Her research interests include base station microgrids energy management, energy trading, scheduling, and energy efficiency optimization.



Kang Li (Senior Member, IEEE) received the B.Sc. degree in industrial automation from Xiangtan University, Xiangtan, China, in 1989, the M.Sc. degree in control theory and applications from the Harbin Institute of Technology, Harbin, China, in 1992, and the Ph.D. degree in control theory and applications from Shanghai Jiaotong University, Shanghai, China, in 1995. He also received the D.Sc. degree in engineering from Queen's University Belfast, Belfast, U.K. in 2015. He currently holds the Chair of Smart Energy Systems at the University of Leeds, U.K. He has authored/co-authored more than 200 journal publications and edited/co-edited 18 conference proceedings, winning over 20 prizes and awards. His research interests include nonlinear system modeling, identification, control, and machine learning, with substantial applications in energy and power systems, transport decarbonization, and energy management in energy intensive manufacturing processes.



Li Zhang (Senior Member, IEEE) received the Ph.D. degree in communications from the University of York, York, U.K., in 2003. She is currently an Associate Professor and leads the Wireless Communication Group with the School of Electronic and Electrical Engineering, University of Leeds, Leeds, U.K. Her research interest includes wireless communications and signal processing techniques, such as massive MlMO, mm-Wave communications, heterogeneous networks, device to device communications. and 5G systems. Since 2006, she has been serving on the Technical Programme Committees of most major IEEE conferences in communications. She is an Associate Editor for the IEEE journal. In 2006, she became a Fellow of the Higher Education Academy. In 2011, she was the recipient of IEEE exemplary Reviewer. In 2012, she was promoted as senior IEEE Member.